# Chapter 2 - Sub-dendritic synapse targeting and postembryonic dendritic geometry remodeling of an identified neuron subserve its changing behavioral role

## 2.1 Abstract

Are the geometries of a dendritic trees and sub-cellular synapse distribution within these trees optimized to affect a neurons input output computations and thereby network and whole brain function? Due to difficulties in determining sub-dendritic input synapse distributions and in relating dendritic geometry to behavioral function only few data exist to address this question. In holometabolous insects, like the moth *Manduca sexta*, structure and function of individually identifiable central neurons are changes during metamorphosis, allowing for studies that directly relate dendritic geometry to behavioral function. Here we show that the functional transformation of the individually identified motoneuron 5 from a slow larval crawling into a fast adult flight motoneurons is accompanied by dendritic remodeling and distinct changes in sub-dendritic targeting of GABAergic inputs. Sub-cellular synapse targeting occurs in a stage specific manner and is not a function of neuropil structure but must rely on specific sub-dendritic recognition mechanisms. Computational models taking the neurons' 3 dimensional geometry into account indicate that dendritic geometry is modified adequately during postembryonic development to meet changing behavioral requirements, and that sub-dendritic synapse targeting yields different input-output computations than random synapse distributions.

## 2.2 Introduction

During brain development a large number of neurons have to be connected appropriately to form the complex neural circuitry essential for adequate brain function. On the single neuron level hundreds or thousands of input synapses are scattered throughout the dendrites. Both, dendritic geometry and the distribution of synapses through the dendrites may affect integration and output computations (Koch and Segev, 2000). However, only few examples indicate that dendritic geometry might be tuned towards behaviorally relevant computations (Single and Borst, 1998; London and Haeusser, 2005). Furthermore, it remains mostly unclear whether synapses are targeted to identifiable sub-dendritic domains of individual neurons, and whether such targeting

might play an important role for behaviorally relevant computations? An alternative possibility could be that evolution has acted to maximize the density of synapses (Chklovskii et al., 2000) at any given unit length of dendritic cable.

Sub-cellular targeting of synaptic inputs takes place in neocortex, where different types of GABAergic inputs are directed to the perisomatic and the distal dendritic regions of pyramidal neurons (Somogyi et al., 1998; Di Cristo et al., 2004). Input targeting to the perisomatic region is crucial for temporal input integration (Pouille and Scanziani, 2001), but the behavioral consequences remain unknown. Similarly, with regard to excitatory inputs the number of AMPA-type glutamate receptors is increased at distal dendrites of pyramidal cells (Stricker et al., 1996; Magee and Cook, 2000; Andrasfalvy and Magee, 2001). Such findings suggest rules for synapse distribution along the proximal to distal dendritic dimension. Moreover, even individual dendritic branches may have distinct molecular compositions, rendering very precise sub-dendritic targeting possible (Horton and Ehlers, 2003). Sub-tree specific synapse distribution may contribute to computational processes by compartmentalization of a neurons' dendritic tree into a multiunit system (Rabinowitch and Segev, 2006). Do complex dendritic trees exhibit distinct addresses for sub-dendritic input synapse targeting, and are dendritic architecture and synapse distributions of importance for adequate input-output computations?

To address this question we combined high resolution confocal laser scanning microscopy (CLSM) with precise 3-dimensional dendritic surface reconstruction (Schmitt et al., 2004) and automated co-localization analysis to map the distribution of potential input synapses through entire dendritic trees (Evers et al., 2005). The concept of 'potential synapses' derives from the fact that contact between axons and dendrites is necessary to form an actual synapse (Stepanyants et al., 2002; Stepanyants and Chklovskii, 2005). We fully employ CLSM resolution to map the contacts of GABAergic terminals onto dendritic surface reconstructions, obtained from intracellular stainings of the motoneuron 5 (MN5) in the ventral nerve cord of the moth, *Manduca sexta*. The use of an insect preparation allows for relating dendritic architecture and intricate sub-dendritic synapse distribution rules to behavioral function. MN5 can be individually identified from animal to animal, even between different developmental stages. During metamorphosis, synaptic input and dendritic structure are remodeled

while MN5 becomes transformed from a slow crawling into a fast flight motoneuron (Duch and Levine, 2000). Therefore, postembryonic changes of dendritic geometry and synapse distribution rules can be related to developmental changes in function.

## 2.3 Material and Methods

### 2.3.1 Animals

*Manduca sexta* were obtained from a laboratory culture reared on artificial diet (Bell and Joachim, 1976) under a long-day photoperiod regime (17/7 h light/dark cycle) at ~26°C.

Both chronological and morphological criteria were used for staging of animals (Bell and Joachim, 1976; Reinecke et al., 1980; Tolbert et al., 1983). In summery, L5 represents an animal from the fifth larval instar and P0 the day of pupal ecdysis. Pupal life was divided into 18 stages, each of which lasted approximately one day. In this study the stages L5, P0, P4 and adult were used. Dissection and intracellular recording were performed as described in Duch and Levine (2000).

### 2.3.2 Intracellular labeling, immuncytochemistry, image acquisition and quantitative morphometry

Intracellular staining and immunohistochemistry were conducted as described in Duch and Levine (2000) and Evers et al. (2006). Briefly, for intracellular labeling of MN5 a thin walled glass microelectrode (25-35 MΩ tip resistance) was filled with a mixture of 7 % Neurobiotin (Linaris GmbH, Wertheim-Bettingen, Germany) and Rhodamin-Dextran (Invitrogen, Carlsbad, CA, USA) in 2 M potassium acetate. An air bubble was left between the dye filled tip and the shaft filled with 2 M potassium acetate to avoid dye dilution. Following intracellular penetration of MN5 (identified by antidromic spike initiation via extracellular nerve 1 stimulation) the dyes were injected iontophoretically by a constant depolarizing current of 3 nA for 45 to 60 minutes. Then the electrode was removed, the ganglia where fixed in 4% paraformaldehyde in phosphate-buffer solution (PBS, 0.1M) for 2 h at room temperature. Ganglia were washed in PBS (0.1M) six times for 15 minutes each. Then tissue was treated in a conventional microwave at 750 W for 2 times at 4° C to enhance antibody penetration and binding. This was followed by additional 2 washes in 0.1 M PBS for 15 minutes each and dehydration in an ethanol-series (50, 70, 90, and 2 times 100 %, 15 minutes each). Preparations were treated in a 1:1 mixture of pure ethanol and methyl salicylate for 5 minutes and cleared in

methylsalicylate. This was followed by 5 minutes treatment in a 1:1 mixture of pure ethanol and methyl salicylate, rehydration in a descending ethanol series, 4 washes in PBS-triton x (0.5 % triton in 0.1 M PBS). Primary antibody incubation with anti-SynapsinI (SynOrf1, kindly provided by Prof. Buchner, University Würzburg; 1:100) and anti-GABA (Sigma-Aldrich Chemie GmbH, Schnelldorf, Germany; 1:400) were conducted for 36 hours in PBS-triton x (0.3 %). This was followed by 6 washes in PBS (15 minutes each) and incubation with secondary antibodies. Neurobiotin was visualized with Cy2-streptavidin (Invitrogen, Karlsruhe, Germany; 1:750); GABAergic processes were visualized by incubation with Cy3-coupled mouse anti-Rabbit (Jackson Immunochemicals Inc., Suffolk, UK; 1:200), and synaptic terminals were visualized by incubation with Cy5-coupled rabbit anti-Mouse antibody (Jackson Immunochemicals Inc.; 1:200). This was followed by 6 washes in PBS (0.1 M), dehydration in an ethanol series (see above), 5 minutes treatment in a 1:1 mixture of pure ethanol and methyl salicylate and clearing and mounting in methyl salicylate.

### 2.3.3 Data acquisition

Images were acquired with a Leica TCS SP2 confocal laser scanning microscope (Bensheim, Germany) using a Leica HCX PL APO CS 40x oil immersion objective (numerical aperture 1.25). To prevent crosstalk between overlapping fluorescent emission wavelength sequential scanning mode was used. Cy2 and Cy5 were scanned simultaneously by using excitation wavelengths of 488 nm (argon laser) and 633 nm (helium neon laser). Cy2 emission was detected between 495 and 530 nm, and Cy5 emission was detected between 640 and 670 nm. No cross-talk between the channels was detected. Cy3 was excited with a green neon laser at 543 nm and detection wavelength was between 550 and 590 nm. Switching between Cy3 scanning and Cy2/Cy5 scanning was conducted after every frame.

By optimizing the sample preparation procedure as described previously (Evers et al., 2005), we can discriminate structures with a diameter of below the emitting wavelength, approaching the theoretical limit of half the emitting wavelength (300 nm), at least in *XY* (Evers et al., 2005; 2006). The smallest dendritic diameters we find in MN5 are above 400 nm diameter. Electron microscopy of Manduca thoracic motor neuropil at the developmental stages relevant for this study demonstrates that synapsin I immunolabeled synaptic terminals appear as distinct puncta of 300 to 3000 nm diameter (Hohensee et al., 2007). Therefore, precise 3-dimensional reconstructions of dendritic

surface (see below) can be used to map the distribution of immunolabled synaptic terminals onto the dendrites of identified motoneurons.

### 2.3.4 Image analysis

Confocal image stacks were further processed with Amira-3.1.1 software (TGS). We used custom developed Amira plugins for 3-dimensional reconstruction of dendritic segments as published previously (Schmitt et al., 2004; Evers et al., 2005). These deliver precise quantification of midline and diameter as well as a triangulated surface definition fully exploiting optical resolution. To address the distribution of putative input synapses into the dendritic tree of MN5, immunolabeled synaptic profiles were used. For quantification of the distribution of immunolabeled profiles along dendrites, the generated surface description was used to calculate the staining density within 300 nm from each surface element, a triangle. The position of the triangle was determined perpendicular to the midline of the corresponding reconstructed segment (for details see Evers et al., 2005). A recent electron microscopy study demonstrated that this procedure accounted for all synaptic terminals located in the thoracic motor neuropils of Manduca, but that it produced approximately 20 percent false positive synapses if only one immunolabel was used (Hohensee et al., 2007). In this study this procedure was done for two immunolabels, anti-synapsin-I and anti-GABA. The correlation of both was used to indicate sites of putative GABAergic input synapses. Snapshots of scenes rendered in Amira-3.1.1 are arranged into figures with Adobe Illustrator CS and Photoshop CS (Adobe Systems Incorporated).

For statistical analyses, morphological parameters exported as ASCII-tables generated from Amira were imported into R (R Development Core Team, 2004). Statistical analysis was conducted with the programs Statistica (StatSof, Hamburg, Germany) and Microsoft Excel. Anova with Newman Keuls post hoc comparison were used to test for statistical differences among multiple experimental groups or multiple classes of dendrites, e.g. between dendrites located in different Sholl spheres. Student's $t$ test was used for comparisons of morphometric parameters between the larval and the adult MN5.

### 2.3.5 Morphometric analysis

The overall structure of MN5 is depicted in figures 1A to D. MN5 is a unipolar cell. The axon projects through the mesothorac nerve 1, and the cell body is located on the

contralateral side of the ganglion. Axon and cell body are connected by a large primary neurite (link segment) from which all major dendritic branches arise. Therefore, the integrative zone might be spread along the major primary neurites from the cell body up to the origin of the axon. To account for this feature in our morphometric analysis, we defined all dendritic branches originating

from the primary neurite as $1^{st}$ order braches, virtually eliminating the link segments (which are treated as 0 order branches / branch points) between cell body and axon, and therefore

collapsing the reconstruction onto one virtual origin. Values referred to as relative to the collapsed origin therefore regard the distance or order on the respective subtree up to its insertion into the cell body – axon link segments. Distances stated as along tree distance are measured as path length from the 0 order branch of the subtree along the midlines of the reconstruction. Air distance values refer to the straight line length in 3dimensional space to the 0 order branch point of the subtree.

### 2.3.6 Synaptic density counts

Density counts for synaptic terminals were conducted in volumes of the following dimensions: 50 x 50 x 12.3 µm (xyz). Within each cube the number of GABA- and synapsin I immunopositive voxels was counted using ImageJ software (NIH) with a plugin that combines intensity threshold segmentation with a 3D connected components extraction (3D objects counter by Fabrice Cordelières, Institut Curie, Orsay, France; ImageJ). Image segmentation of complex immunodata, i.e. assigning a certain voxel as signal respectively background, will hardly ever be absolutely accurate. In contrast, it is rather an optimization task that estimates the best approximation to a given staining pattern. Since neither pattern nor intensity based algorithms are universally applicable, we here compared the outcome of two approaches to estimate the data integrity. In a first approach, manual threshold was determined by a third person using a threshold mask in ImageJ without knowledge of the type of the immunostaining and the developmental stage. This analysis was conducted blindly for all cubes. Additionally, a second standardized method was applied to define thresholds automatically. For each immunostaining the staining intensity of all voxels within a cube was plotted as a frequency distribution intending to find the noise peak of each staining within the different images of GABA and Synapsin I. After removal of depth dependent background alterations with a rolling ball algorithm, the noise peak (offset/ detector/

technical noise) was found within the first 10 grey values for all image stacks (grey scale: 0 to 255). For the purpose of finding a conservative approach to eliminate slight fluctuations of the voxel intensity, graph 10er bins have been created. Normalization has been done to the first bin (which represents background). Thereby a normalized voxel frequency distribution is achieved and threshold for accepting a voxel as immunopositive in a conservative manner was defined as brightest 10 percent of all voxels. In all cubes the frequency distribution was steep at this 10 percent value. This represents a good approximation for the transition from signal to background.

### 2.3.7 Multi-compartment modeling

Theoretic modeling of the passive integration of electric discharges of dendritic trees has been done in Neuron. The import of the reconstructed geometries of MN5 at different developmental stages into Neuron was done as described earlier (Evers 2005). Due to the lack of accurate values for the passive electrical properties of Manduca motorneurons, we used values commonly applied for vertebrate and invertebrate neurons (specific membrane capacity $cm=1.15*10^{-6}$ $F*cm^{-2}$, axoplasmatic resistance $Ra=45ohm*cm$) with following passive leak conductance $g\_pas=0.0001667$ $ohm^{-1}$ $com^{-2}$, and equilibirum $e\_pas=-65mV$).

Synapse localization probabilities determined as described above were transformed into a discrete map of synaptic localizations as follows. To randomize synaptic positioning with the constraints of the specific synaptic distribution characteristics, we used a random number generator (equal distribution). We normalized to the total length of the dendritic arbor to position a given number of synapses on the reconstructed dendritic arbor. A value of 40% of the maximum synaptic likelihood (as determined in the individual data set) was used as the positive criterion to confirm synapse localization, and synapses at positions with lower synaptic likelihood were removed and redistributed. The synaptic firing onset was randomized for each individual synapse to fire once during a simulation, so that the synaptic activation sequence followed a gaussian distribution with a given width (sigma) and its

center to be at 10ms after the start of the simulation. Synaptic activations were realized with NEURON's AlphaSynapse model (tau = 0.8ms, equilibrium potential e = -10mV and maximum conductivity $g=10^{-7}$ $Ohm^{-1}$). To scale the size of the larval dendritic tree to match the adult length, we changed each dendritic branch length by multiplication

with the ratio of total adult to total larval tree length. All modeling results were exported as ascii files and analyzed within R (http://www.r-project.org).

## 2.4 Results

For a quantitative comparison between the branching geometry of the larval and the adult MN5 dendritic tree, 3-dimensional reconstructions (Fig 1C, D) were made from confocal image stacks (Fig 1A, B). Postembryonic changes in the structure of MN5 have previously been described qualitatively (Duch and Levine, 2000), and quantification has been conducted by manual reconstruction (Libersat and Duch, 2002), but a thorough quantitative analysis based on improved novel semi-automatic reconstruction tools (Schmitt et al., 2004; Evers et al., 2005) has been lacking.

Clearly, the postembryonic development of MN5 from a larval crawling into an adult flight motoneuron is accompanied by a significant increase in total dendritic length (adult: 39716 ± 3838 µm; larva: 26227 ± 267 µm (Fig 1E)). This is caused by increases in the mean length of the individual dendritic branches from 4.12 ± 1.17 to 5.01 ± 1.04 µm (Fig 1F) and by an increase in the number of dendritic branches (adult: 8413 ± 2238 dendritic branches; larva: 6577 ± 1696 dendritic branches; Fig 1 G). In addition the mean radius of the individual dendrites is increased significantly from 0.28 ± 0.09 to 0.34 ± 0.07 µm (Fig 1H).

The pervasion of the neuropil by the dendritic tree of MN5 can be assessed by calculating the relative space occupied by all dendrites within the volume defined by the 3-dimensional perimeter of the dendritic field. We define this value as dendritic density. Dendritic density is almost twice as big in the adult as compared to the larval stage (Fig 1I), because maximum dendritic path lengths are similar between both stages, but the number, mean length and mean radius of the dendrites are increased in the adult MN5. The increase in the number of dendrites is mostly caused by adding dendrites in the branching orders 1 to 20 in the adult MN5 (Fig 1J). A first order dendrite is defined as any dendrite branching off the primary neurite which connects the cell body and the axon in MN5 (see figures 1A, B). A second order branch is defined as any dendrite branching off a first order branch, and any dendrite branching off an n-order dendrite is defined as n + 1 order dendrite (see methods). The adult MN5 also contains more dendrites in the branch orders 20 to 40, but in higher orders (40 to 75) the number of dendrites is similar between the larval and the adult MN5 (Fig 1J). The mean radius of the individual dendritic branches is larger in adult than in the larval MN5 (Fig 1H). This
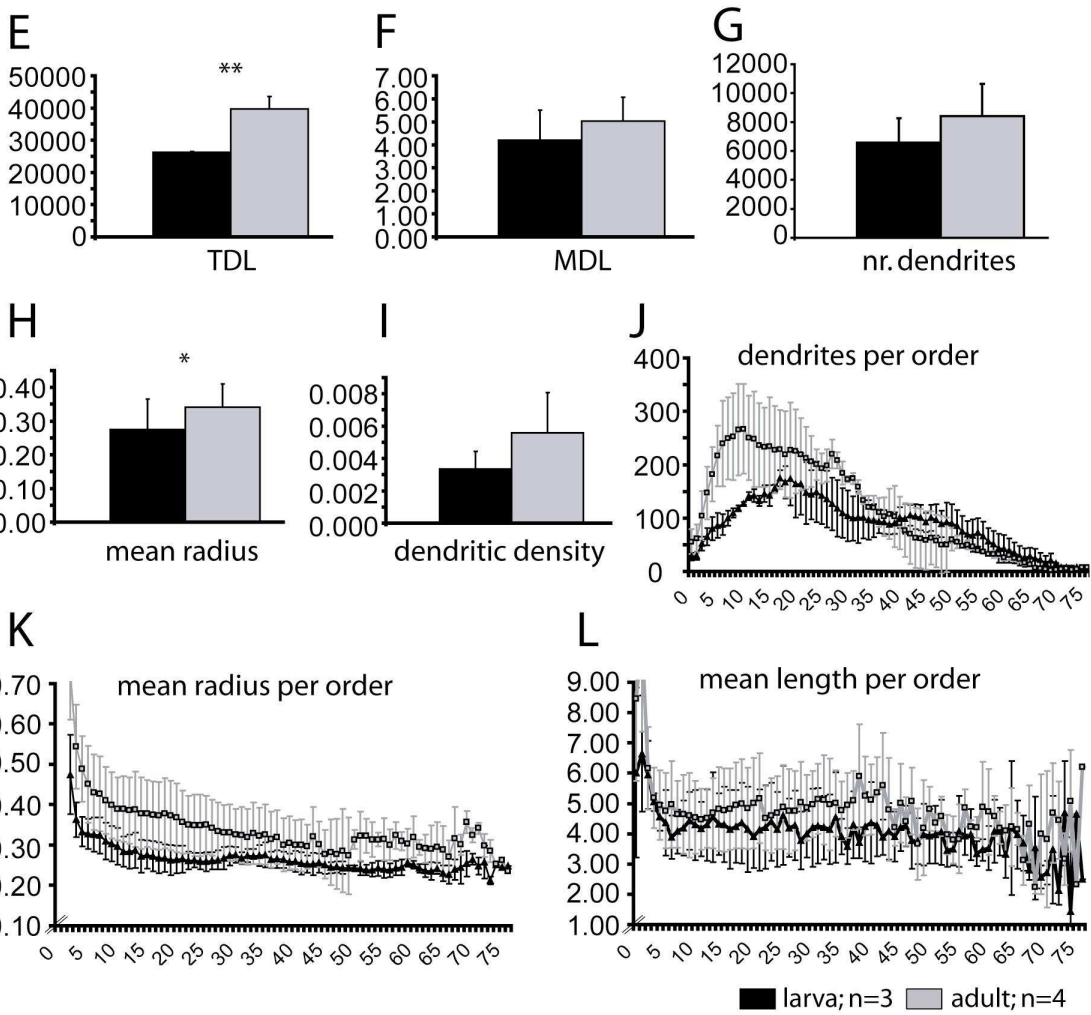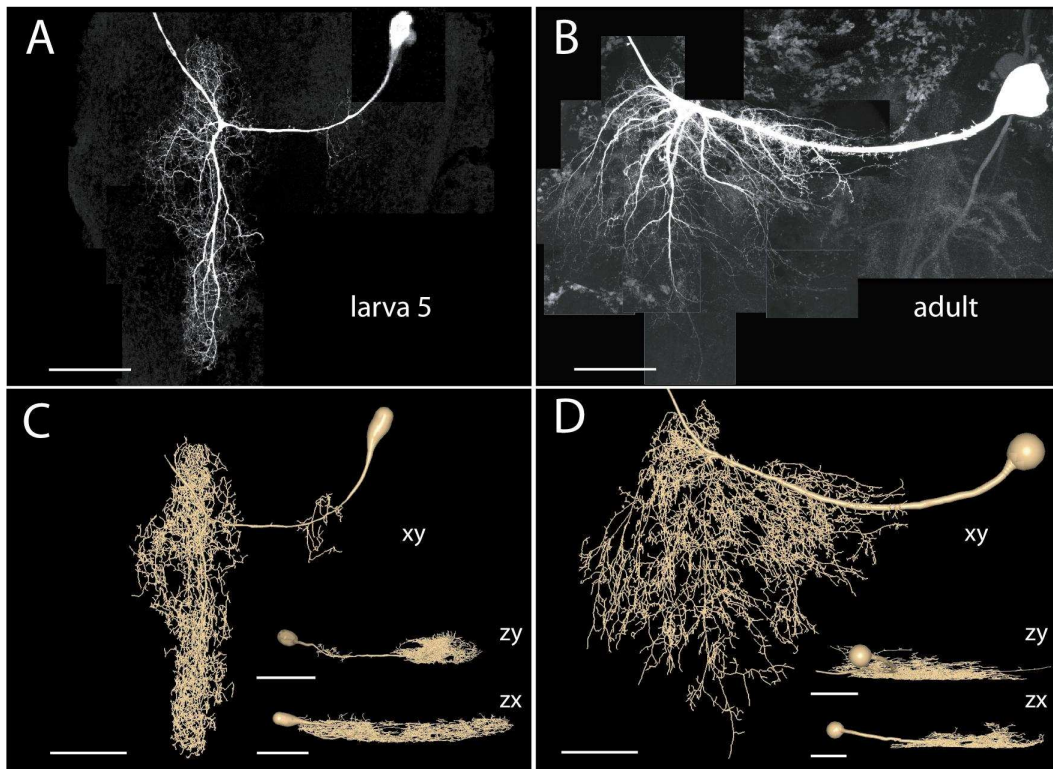
A — larva 5

B — adult

C — xy, zy, zx

D — xy, zy, zx

E — TDL **

F — MDL

G — nr. dendrites

H — mean radius *

I — dendritic density

J — dendrites per order

K — mean radius per order

L — mean length per order

larva; n=3    adult; n=4

**Figure 1.** *Morphometric comparison of the larval and the adult MN5*
Representative confocal images of the larval (A) and the adult (B) MN5. Both images are projections views of all optical sections into one focal plane to visualize all central projections in one overview image. The cell body (cb) is located contralateral to the axon, and both are connected by a primary neurite which also gives rise to all major dendritic branches. Images of 3 - dimensional reconstructions are depicted in (C) for the larval MN5 and in (D) for the adult MN5. Both cells are shown in xy-, zy- and zx-view. Quantitative morphometric parameters as averaged from 3 representative larval (black bars, black triangles) and 4 representative adult (grey bars, grey triangles) reconstructions are shown in D to L. Total dendritic length (TDL) is significantly increased in the adult MN5 (E). Mean dendritic length (MDL) (F), the number of dendrites (G) and dendritic density (I) are higher in the adult than in the larval MN5 but these differences are not statistically significant. Mean dendritic radius (H) is larger in the adult as compared to the larval MN5. Branch order analysis shows that the number of dendrites (J) of the adult MN5 is much higher in all branch orders as compared to the larval MN5, but peaks in the branch orders 5 to 35. In the adult MN5 mean dendritic radius (K) higher in all branch orders as compared to the larval MN5. Mean dendritic length (L) is increased in the adult in the branch orders 15 to 45, but is similar in the larval and the adult MN5 throughout all other branch orders. Statistical significance was tested with unpaired student's t-test, ** indicate $p < 0.01$, * indicate $p < 0.05$ . Scale is 100 µm.

increase in mean dendritic radius is caused by an increase of the radius of dendrites through all branch orders, and is therefore not caused by an increase of the diameter of particular dendrites only (Fig 1K). The increase of mean dendritic length (MDL) in the adult (Fig 1F) is entirely caused by an increase in mean dendritic branch length in the branch orders 15 to 45, but MDL is similar in the larval and the adult MN5 through all other branch orders (Fig 1L).

Remodeling dendritic structure during postembryonic development is directly related to changes in synaptic inputs impinging onto the motoneurons dendritic tree (Consoulas et al., 2000; Tissot and Stocker, 2000; Weeks, 2003). For MN5 in Manduca it has been shown that larval synapses are eliminated during disassembly of larval crawling circuits, and MN5 dendrites retract during late larval and early pupal life (Duch and Mentel, 2004). This is followed by dendritic growth and synaptogenesis during the motoneuron's integration into the newly formed adult flight motor networks (Duch and Levine, 2000; Evers et al., 2006). Postembryonic changes in dendritic architecture, membrane currents and motor function have been described for MN5 (Duch and Levine, 2000). This renders MN5 a useful model to ask whether postembryonic changes in the structure and function of individual neurons are accompanied by stage-specific rules for sub-cellular targeting of synaptic inputs through complex dendritic trees. In principle, stage-specific input-output computations of dendritic trees could be aided by function-specific synapse placement. An alternative possibility is that neuronal shape is

optimized to minimize the length of wire and to maximize the density of synapses (Chklovskii et al., 2000; Chen et al., 2006).

To address the question of function-specific synapse placement versus wiring optimization for all presynaptic neurons of one transmitter class impinging on the dendrites of MN5, we examined the distribution of the GABAergic input sites on the dendritic tree of MN5. We conducted immuno-labeling against the general presynaptic protein synapsin I and for the neurotransmitter GABA, whereby the co-localization of both labels highlights a GABAergic release site (see methods, Evers at el., 2005). In the insect CNS anti-synapsin I immunolabeling can be used as reliable marker for synaptic terminals (Watson and Schuermann, 2002) and yields puncta of 300 to 3000 nm diameter which represent the synaptic terminal including active zone plus reserve vesicle pool (Hohensee et al., 2007). Combining these immunolabels with an intracellular staining of MN5 allowed us to assess the distribution of GABAergic release sites in relation to the dendritic arbor of MN5. To localize and quantify the juxtaposition of presynaptic sites to the dendritic arbor, we used recently developed tools to analyze confocal image stacks at the limit of optical resolution (Schmitt et al., 2004; Evers et al., 2005, see methods). Briefly, the cell surface of the neuronal arborization is reconstructed from confocal image stacks, and the co-localization probability of GABA and synapsin-I is calculated for each surface element within a 300nm distance.

Using this method we charted the distribution pattern of GABAergic input synapses onto the dendritic tree of MN5 at different developmental stages (Fig 2). As an example, in figure 2A1 a single reconstructed dendritic branch is superimposed on an optical section from a whole-mount immunostained neuropil against GABA neurotransmitter (green). Every surface element of the dendrite reconstruction is color coded for the mean GABA-immunolabel staining intensity within 300 nm distance. In figure 2A2 the corresponding optical section of the anti-synapsin I immunolabel (blue) is shown accordingly. Parts of the dendritic surface reconstruction with an anti-synapsin I label within a 300 nm distance to the dendritic surface are coded by warmer colors, indicating a putative input synapse. To highlight synaptic terminals which contain GABA, we calculated a correlation coefficient of both, the anti-GABA- and anti-synapsin I image data. We extracted the average correlation value within 300nm distance to the neuronal surface in order to restrict the analysis to GABAergic synapses only which are in
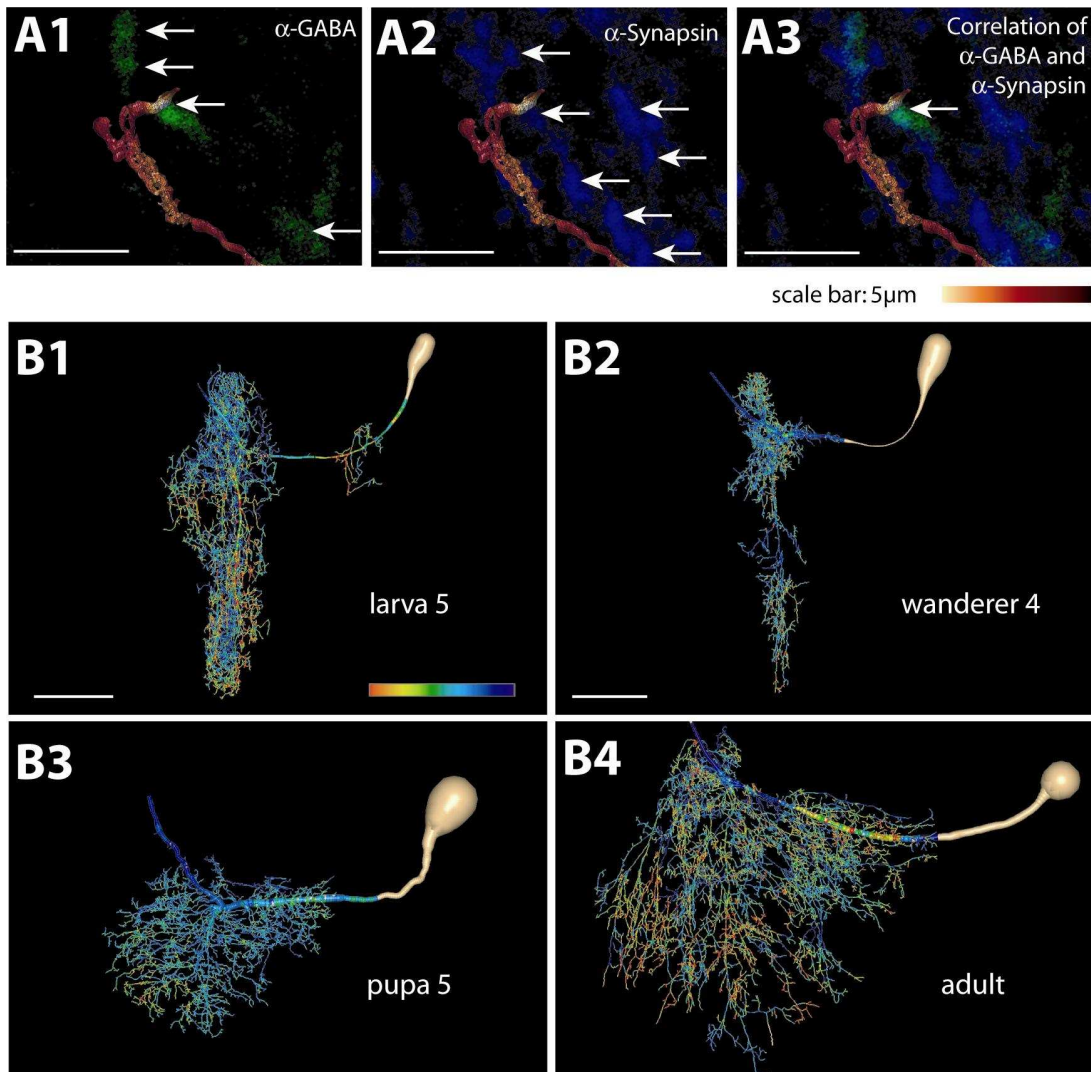
**Figure 2.** *Mapping of putative GABAergic inputs onto the dendritic surface of MN5*
The surface of MN5 is reconstructed from confocal image stacks, and the co-localization probability of GABA and synapsin-I is calculated for each surface element within a 300nm distance. The method is exemplified in (A) with a selective enlargement of one optical section through one dendritic arbor. First, the surface reconstruction is superimposed on a single optical section of anti-GABA immunostaining (green, A1). Each element of the surface reconstruction is color coded for the mean GABA-immunostaining intensity within 300 nm distance, with warmer colors indicating higher anti-GABA staining intensity. The same procedure is shown for anti-synapsin 1 immunostaining from the same optical section (A2). The correlation of both mappings is depicted in (A3). This method is applied for the entire dendritic tree of the larval MN5 at the stages larva5 (B1), wandering 4 (B2), pupal stage 5 (B3) and the adult (B4). Scale is 100 µm.

juxtaposition to the dendritic surface of MN5 (Fig 2A3). Applying this procedure to all optical sections produced a complete map for the distribution of putative GABAergic input synapses onto the entire dendritic tree (Fig 2B). We have previously demonstrated that relative synapse numbers detected with this method correlate with

electrophysiological analysis of the numbers and amplitudes of postsynaptic potentials (Duch and Mentel, 2004). A correlative electron- and confocal microscopy study in the Manduca CNS also demonstrates the validity of this procedure (Hohensee et al., 2007).
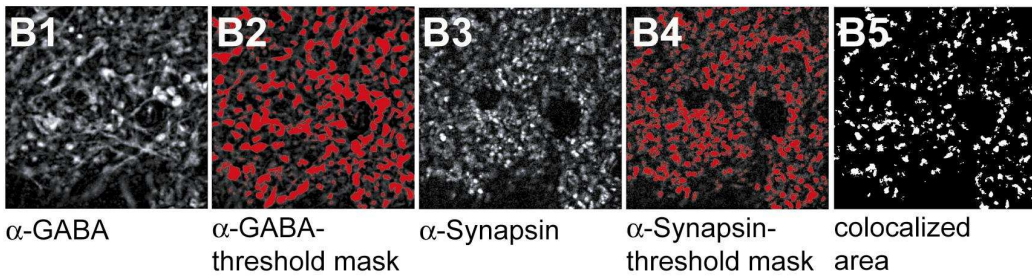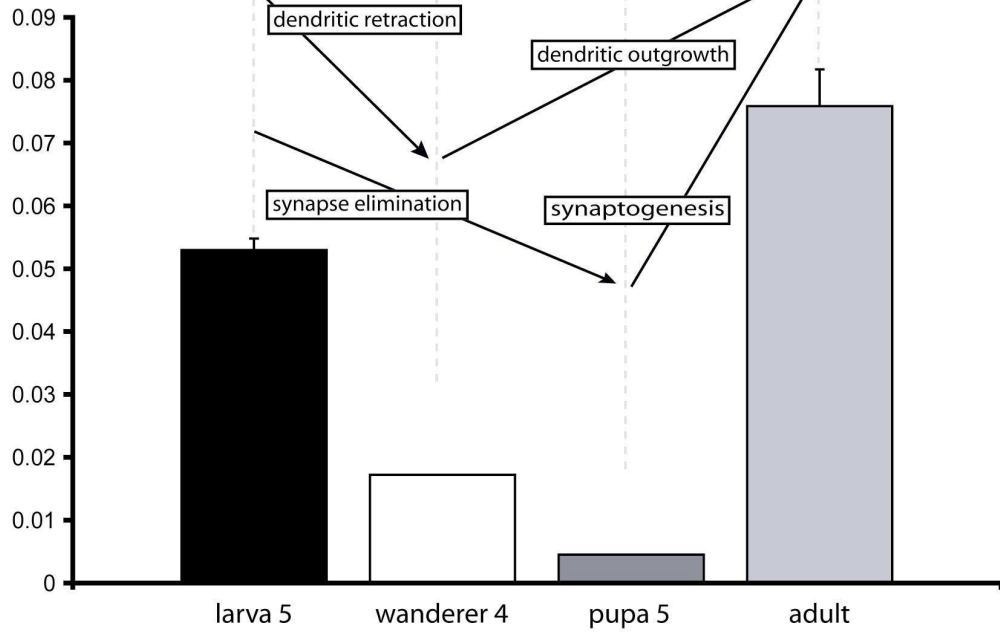
Before testing for site specific sub-dendritic input synapse targeting, the overall amount of putative GABAergic inputs per dendritic surface was compared between different stages of postembryonic development to address two questions. First, is the density of putative GABAergic contacts similar in the larval crawling and in the adult flight MN5, or do different motor task require different amounts of GABAergic input? And second, do dendritic regression and outgrowth correlate strictly with the elimination and the acquisition of putative GABAergic inputs, or do changes in the number of GABAergic inputs and the number of dendrites follow different time courses? Maps of all putative GABAergic inputs distributed over the dendritic tree of MN5 are shown for the larval stage (Fig 2B1), the day of pupal ecdysis (Fig 2B2), the fifth day of pupal life (Fig 2B3), and for the adult stage (Fig 2B4). These data are quantified and normalized by dividing the dendritic surface area contacted by putative GABAergic terminals by the total dendritic surface area for each of the four developmental stages (Fig 3A). More than seven percent of the dendritic surface of the adult flight MN5, but only five percent of the dendritic surface of the larval crawling MN5 receives putative GABAergic input (Fig 3A). This difference is statistically significant ($p < 0.01$, students T-test), indicating that flight spiking patterns might require more inhibitory inputs per dendritic surface than larval crawling spiking patterns. The regression of larval dendrites between the fifth larval instar (Fig 2B1) and the day of pupation (wanderer 4, Fig 2B2) is accompanied by synapse elimination (Fig 3A) as has previously been demonstrated (Duch and Mentel, 2004). However, the regressed dendritic field at stage W4 contains not only fewer putative GABAergic inputs than the larval dendritic tree, but at stage W4 a smaller portion of the dendritic surface (1.7 percent) is contacted by putative GABAergic terminals than at the larval stage (5.3 percent; Fig 3). This indicates that during late larval life putative GABAergic synapses are eliminated also from dendrites that have not retracted. During the initial phase of rapid dendritic growth within the first 5 days of pupal life (Evers et al., 2006) the color coded reconstruction indicates only few new putative GABAergic inputs (Fig 2B3). As a result the relative dendritic surface area contacted by putative GABAergic input synapses at pupal stage P5 (0.004 percent) is nearly eliminated compared to stage W4 (1.7 percent; Fig 3). This demonstrates that

newly formed dendrites between the stages W4 and P5 are not immediately contacted by GABAergic terminals. The second phase of dendritic growth and maturation between pupal stage 6 and adult (Duch and Levine, 2000; Evers et al., 2006) is accompanied by the formation of many new putative GABAergic inputs (Fig 2B4), so that the percentage of dendritic surface area in contact with putative GABAergic input synapses increases more than six-fold between pupal stage 5 and the adult stage (Fig 3). These data demonstrate that the portion of dendritic surface area that receives putative GABAercic input changes during dendritic regression and outgrowth, and thus, GABAergic synapse elimination and acquisition are not simply consequences of dendritic regression and new outgrowth. Furthermore, the density of GABAergic terminals contacting the dendritic surface of MN5 is significantly lower in the larval crawling versus in the adult flight MN5. This could either be caused by a higher overall density of GABAergic terminals in the adult motor neuropil, or alternatively, more GABAergic terminals might specifically contact the adult dendritic tree as compared to the larval dendritic tree at similar overall synapse densities at both stages. The latter would require specific mechanisms to target more inhibitory synapse to the adult dendritic tree as compared to the larval dendritic tree of MN5.
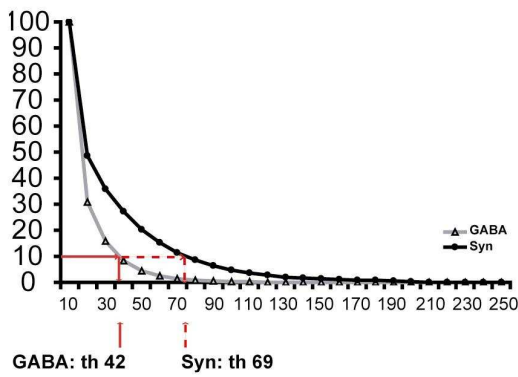
To distinguish both possibilities, we counted the relative numbers of GABAergic terminals and total terminals in defined volumes in the larval and in the adult motor neuropil. Within the perimeter of the dendritic field of MN5 terminals were counted in three cubes of defined side length (see methods). Within each cube the number of GABA- (Fig 3B1) and of synapsin (Fig 3B3) I immunopositive voxels were counted and divided by the total number of voxels. Thresholds for immunopositive voxels were defined with two independent methods. First, manual threshold was determined blindly by a third person using a threshold mask in Image J (NIH, see methods). In addition to determining the thresholds manually, we also employed a second standardized method to define thresholds. For each immunostaining the staining intensity of all voxels within a cube was plotted as frequency distribution. Threshold for accepting a voxel as immunopositive was defined at the brightest 10 percent of all voxels (Fig 3C, see red lines, see methods). In all cubes the frequency distribution was steep at this 10 percent value, representing a steep transition from signal to background. Every voxel count was conducted with both methods (manual blind thresholding and standardized thresholding), and the results were processed separately. Since every GABAergic terminal contains GABA and synapsin I, the overlap of both was used to count voxels
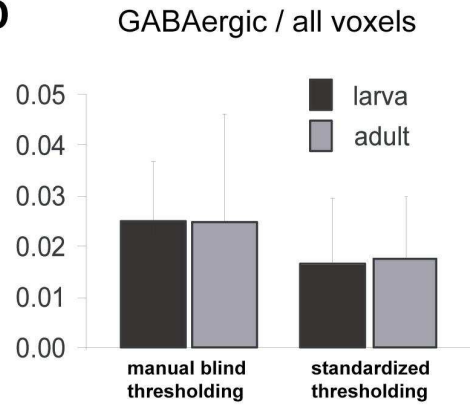
**A**

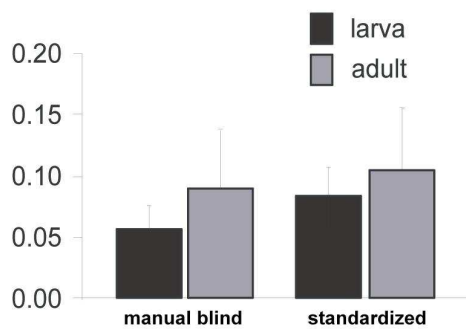number of GABAergic triangles/
total number of surface triangles

dendritic retraction

dendritic outgrowth

synapse elimination

synaptogenesis

larva 5  wanderer 4  pupa 5  adult

**B1** α-GABA

**B2** α-GABA-
threshold mask

**B3** α-Synapsin

**B4** α-Synapsin-
threshold mask

**B5** colocalized
area

**C**

GABA
Syn

GABA: th 42    Syn: th 69

**D** GABAergic / all voxels

larva
adult

manual blind
thresholding

standardized
thresholding

**E** (Syn I - GABAergic) / all voxels

larva
adult

manual blind    standardized

**F** I / E ratio

larva
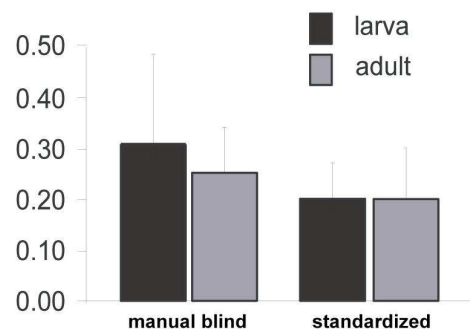adult

manual blind    standardized

**Figure 3.** *The density of GABAergic contacts with MN5 changes through different stages*
(A) shows the number of dendritic surface triangles in contact with a putative GABAergic terminal normalized to the total number of surface triangles for the stages larva 5 (black bar), wandering 4 (white bar), pupa 5 (dark grey bar), and adult (light grey bar). Error bars represent standard deviations. The phases of dendritic regression and dendritic outgrowth as described in Duch and Levine (2000) are indicated by arrows and labeled boxes.
(B) The relative numbers of GABAergic terminals and other terminals within the perimeter of the dendritic field of MN5 (in three cubes of defined volume, see methods) were counted in defined volumes in the larval and in the adult motor neuropil. Within each cube the number of GABA- (B1) and of synapsin I (B3) I immunopositive voxels was counted and divided by the total number of voxels. Thresholds for immunopositive voxels were defined with two independent methods. First, manual threshold was determined blindly by a third person using a threshold mask in Image J (NIH, see methods). Representative blindly defined threshold masks are shown for anti-GABA immunostaining (B2) and for synapsin immunostaining (B4). Co-localization was used to determine voxels belonging to putative GABAergic synapses (white mask in B5). Automated threshold determination is depicted in (C). The staining intensity of all voxels within each cube is plotted as frequency distribution. Threshold for accepting a voxel as immunopositive was defined at the brightest 10 percent of all voxels as indicated by the red lines (C). To determine the number of all voxels located in other than GABAergic synaptic terminals, the number of voxels immunopositive for GABA and for synapsin I were subtracted from the total number of synapsin I positive voxels. To normalize these numbers, each voxel count was divided by the total number of voxels within each cube. (D) shows the percentage of voxels that are GABA immunopositive for the larval (black bar) and the adult (grey bar) motor neuropil as determined with both methods (manual blind and automatic thresholding). Error bars represent standard deviations. Each bar represents the mean of 12 cubes from 4 different animals. (E) shows the respective bar diagram for voxels from putative GABAergic terminals. (F) shows the respective diagram for the ratio of all voxels belonging to putative GABAergic terminals divided by all other synapsin I positive voxels within each cube. No significant differences for any of these voxel counts were found between larval and adult neuropil regions surrounding MN5 dendrites.

located in GABAergic terminals (Fig 3B5, co-localized area). To determine the number of all voxels located in other than GABAergic synaptic terminals, the number of voxels immunopositive for GABA and for synapsin I were subtracted from the total number of synapsin I positive voxels. To normalize these numbers, each voxel count was divided by the total number of voxels within each cube (percentage GABAergic or percentage Syn I positive voxels). The percentage of voxels that are GABA and synapsin I positive is in the larval and in the adult flight motor neuropil. In all cubes, about 2 percent of the three dimensional space is occupied with putative GABAergic terminals, no matter whether manual (Fig 3D, black bars) or standardized (Fig 3 D, grey bars) thresholding is used. The same is true for the percentage of all other terminals containing synapsin I positive immunolabel (all Syn I immunopositive voxels minus all co-localized voxels). This most likely reflects all type I terminals, except GABAergic ones, in the respective neuropil regions. With both methods we find approximately 7-8 percent of the volume of both neuropil regions occupied with non-GABAergic type I terminals (Fig 3E). No statistical differences exist between both regions or between both methods (Students T-

test, p > 0.65). As GABA is the predominant inhibitory transmitter in the insect CNS and most other type I terminals in the ventral nerve cord are cholinergic (Burrows, 1996), an inhibition / excitation ratio (I/E ratio) can be estimated by the ratio of both voxel counts (Fig 3F). The I/E ratio is approximately 0.22, it is similar between the larval and the adult motor neuropil. Only manual thresholding in the larval motor neuropil yields higher I/E values (Fig 3F, 0.31 for manual thresholding in the larva), but this difference is not statistically significant. In summary, these data demonstrate that overall densities of GABAergic and other type I terminals are similar in the larval and in the adult motor neuropil surrounding the dendrites of MN5. Consequently, the observed higher density of putative GABAergic terminals contacting adult MN5 dendrites as compared to larval ones is not a consequence of terminal availability but requires higher targeting or higher maintenance rates for GABAergic synapses on the adult motorneuron dendritic tree.

However, not only dendritic geometry and synapse density, but also the distribution of synapses through the dendrites may affect synaptic input computations and neuronal function (Koch and Segev, 2000). To test whether the postembryonic change in motor function as described for MN5 (Duch and Levine, 2000) is accompanied not only by changes in the amount of putative GABAergic input, but also by stage-specific sub-dendritic synapse placement we examined whether putative GABAergic inputs were scattered randomly throughout the dendritic field or whether rules existed for distributing GABAergic inputs through dendritic fields. To address this question a modified Sholl (Sholl, 1953) analysis was conducted. For Sholl analysis the entire length of the primary neurite that houses dendritic branches is regarded as the origin of the dendritic tree, and is collapsed into one point in space mathematically (Fig 4A, see green outline, see also methods). Consecutive three dimensional concentric spheres of 40 µm radius were placed around this origin of the dendritic tree. To visualize all dendrites belonging to specific Sholl spheres they are depicted in different colors in figures 4B and C (blue, Sholl sphere 40 to 80; red, 120 to 160; green, 240 to 280). Within each Sholl sphere the surface area in contact with a putative GABAergic input synapse is divided by the total surface area in that sphere. This normalizes for differences in dendritic surface area among different Sholl spheres. The GABA-positive fraction of dendritic surface is plotted for each Sholl sphere for both, the larval and the adult MN5 (Fig 4D). For the larval MN5 each Sholl sphere receives the same relative
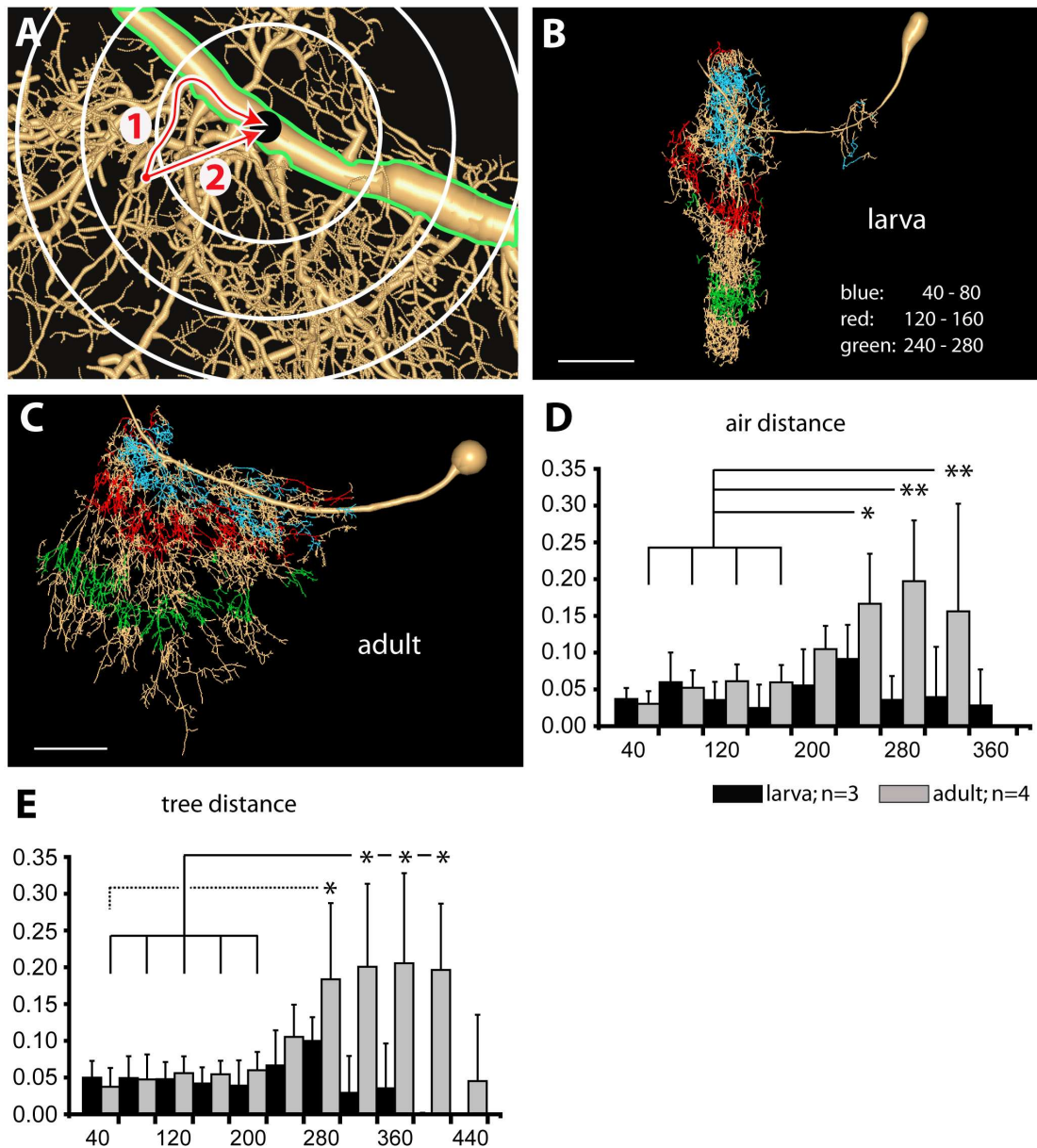
**Figure 4.** *Sholl analysis reveals non-random distribution of putative GABAergic input into the dendritic tree of the adult MN5*

For Sholl analysis the entire length of the primary neurite that connects the axon and the cell body and houses dendritic branches is regarded as the origin of the dendritic tree, and it is virtually collapsed into one point in space (A, see green outline, see also methods). Sholl spheres are defined as consecutive concentric spheres of 40 µm radius around the origin (white circles in A). For visualization different colors signify different Sholl spheres in the larval dendritic tree (B) and in the adult dendritic tree of MN5 (C, blue, Sholl sphere 40 to 80; red, 120 to 160; green, 240 to 280). For normalization the surface area in contact with a putative GABAergic input synapse is divided by the total surface area within each Sholl sphere and plotted as a bar diagram for each sphere (D, E) for the larval MN5 (grey bars) and for the adult MN5 (black bars). In (D) the Sholl spheres are defined using linear distance in 3 dimensional space, and in (E) Sholl spheres are defined using the distance along the midline of the dendrites (see methods). Significant differences between different Sholl spheres are signified by asterisks (ANOVA, Duncan post-hoc test, ** indicate $p < 0.01$, * indicate $p < 0.05$ )

amount of putative GABAergic input throughout all Sholl spheres (Fig 4D, black bars; ANOVA, p = 0.29). By contrast for the adult MN5, a significant increase in the relative amount of putative GABAergic inputs per dendritic surface area occurs in the higher Sholl spheres (Fig 4D, grey bars, 240 -360 µm spheres; ANOVA, p < 0.01). This means that putative GABAergic inputs occur predominantly more distally in the dendritic field. This shift of GABAergic inputs towards the perimeter of the dendritic field of the adult MN5 is also obvious when using actual distance along the run of the dendrites to the origin, instead of air distances, to define the radii of the Sholl spheres (Fig 4E, tree distance, ANOVA, p < 0.01). Tree distance is a more functional measure, because postsynaptic potentials (PSPs) have to propagate along the run of the dendrites to the spike initiating zone. For both air distance and tree distance (ANOVA, p = 0.21) of the larval MN5, the relative dendritic surface contacted by putative GABAergic terminals is similar throughout all Sholl spheres (Figs 4 D, E, black bars). These data demonstrate that the postembryonic change in function of MN5 is accompanied by a change in GABAergic input synapse distribution, from a random distribution in the larval crawling motoneuron to a shift of putative GABAergic inputs towards the more distal dendrites.

In principle this postembryonic re-distribution of putative GABAergic inputs through the dendritic field of MN5 could be caused in two different ways. First, it might simply reflect a general re-organization of the neuropil. In this case distal dendrites would be located within neuropil regions with a higher density of GABAergic terminals than the neuropil regions around more proximal dendrites of MN5. If every putative GABAergic terminal had the same chance to make contact onto a neighboring dendrite, a higher density of terminals would result in a higher input synapse number per dendritic surface area. This case would not require specific sub-dendritic targeting of GABAergic terminals onto MN5. Alternatively, the overall densities in excitatory and inhibitory terminals might be even throughout all neuropil regions surrounding MN5 dendrites. In this case the observed shift of putative GABAergic input synapses towards higher Sholl spheres would require that GABAergic terminals are targeted preferentially to higher order dendrites. This, in turn, would require specific sub-dendritic addresses for targeting these terminals. To distinguish both possibilities, we counted the relative numbers of GABAergic terminals and total terminals in neuropil regions located within lower MN5 Sholl spheres with relatively few GABAergic inputs (Fig 5A, region 1), and compared these to the numbers of GABAergic and total terminals in neuropil regions
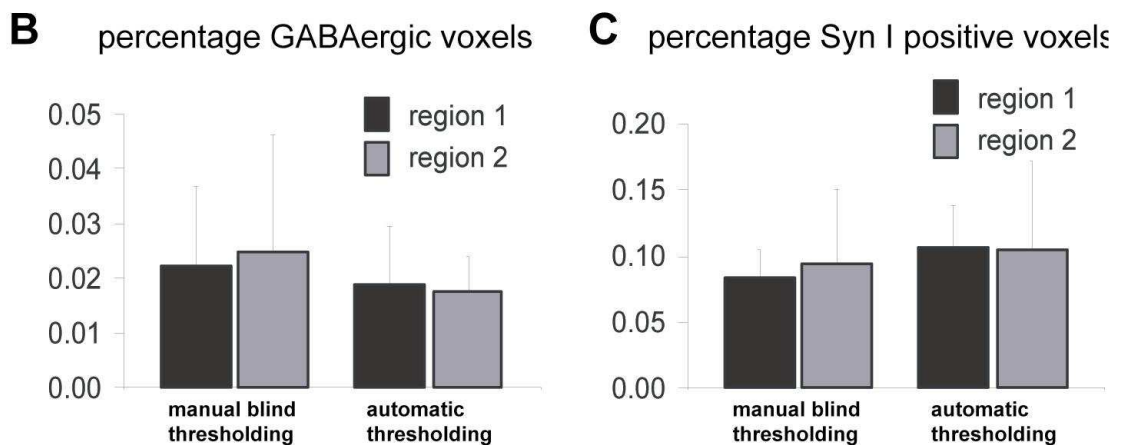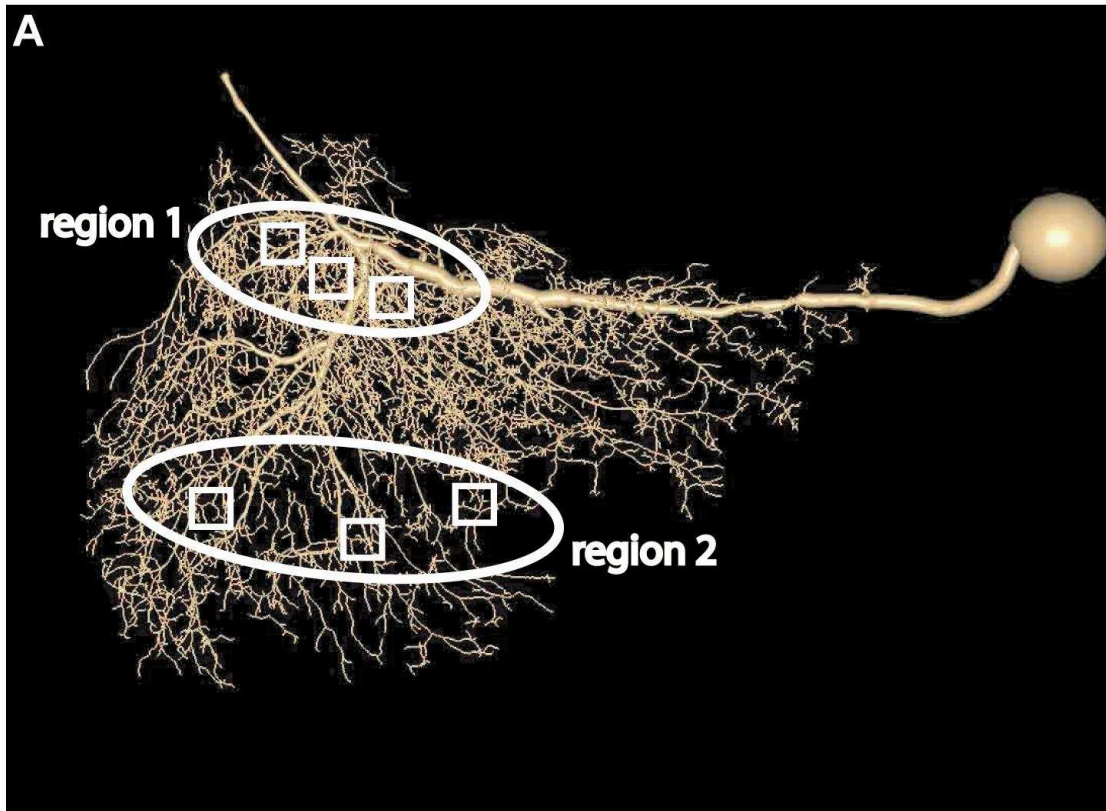
**Figure 5.** *Overall densities of putative synapses in the neuropil are similar between low and high Sholl spheres in the adult*
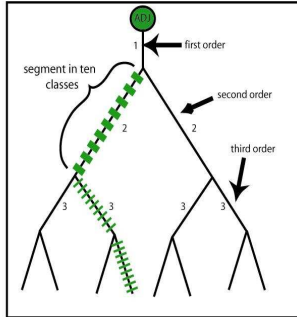
The relative numbers of GABAergic terminals and total terminals were counted and compared between neuropil regions located within lower MN5 Sholl spheres with relatively few GABAergic inputs (A, region 1) and neuropil regions located within higher MN5 Sholl spheres with large numbers of putative inputs impinging on MN5 (A, region 2). Within each region synaptic terminals were counted in three cubes of defined volume (A). Identification of immunopositive voxels for GABA and for synapsin was accomplished by determining labeling intensity thresholds with two different methods as described in the methods and in figures 3B, C. Numbers of immunopositive voxels were normalized by dividing them by the total number of voxel within each cube. (B) shows that for both regions and both thresholding methods the percentage of GABA-positive voxels is approximately 2 percent. (C) demonstrates that for both regions and both thresholding methods the percentage of synapsin I positive voxels is approximately 8 percent. Error bars represent standard deviation. Black bars represent region 1, grey bars represent region 2.

located within higher MN5 Sholl spheres with large numbers of putative inputs impinging on MN5 (Fig 5A, region 2). Within each region synaptic terminals were counted in three cubes of defined volume. Within each cube the number of GABA- and of synapsin I immunopositive voxels were counted. Identification of immunopositive voxels was accomplished by determining labeling intensity thresholds with two different methods as described above (Figs 3B, C). For normalization the number of immunopositive voxels was divided by the total number of voxels within each cube. The resulting percentage of voxels that are GABA and synapsin I positive is similar in region 1 and in region 2. In all cubes, about 2 percent of the three dimensional space is occupied with putative GABAergic terminals, no matter whether manual (black bars) or standardized thresholding (grey bars) is used (Fig 5B). Consequently, the accumulation of GABAergic inputs in higher Sholl spheres of the dendritic surface of MN5 is not caused by an overall higher density of GABAergic terminals in the respective neuropil regions. The same is true for the percentage of all other terminals containing synapsin I positive immunolabel (all Syn I immunopositive voxels minus all co-localized voxels). This most likely reflects all type I terminals, except GABAergic ones, in the respective neuropil regions. With both methods we find approximately 8 percent of the volume of both neuropil regions occupied with non-GABAergic type I terminals (Fig 5C). No statistical differences exist between both regions or between both methods (Students T-test, $p > 0.65$). The resulting I/E ratio is approximately is similar between region 1 and region 2, and no differences are found between both thresholding methods (0.27, data not shown). In summary, these data demonstrate that the dendritic tree of MN5 is embedded into a neuropil that is homogeneous with regard to the density of GABAergic terminals (Fig 5B), the density of type I excitatory terminals (Fig 5C) and the I/E ratio resulting from both. Therefore, the Sholl distributions for GABAergic inputs as observed for the dendritic tree of the adult MN5 (Figs 4D, E) are not a consequence of non-homogenous neuropil structure, but instead, are caused by sub-dendritic targeting of GABAergic terminals preferentially onto higher order dendrites.
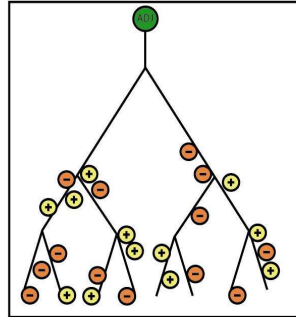
In addition to pushing putative GABAergic inputs towards the perimeter of the dendritic field, are there also specific strategic localizations of such inputs with regard to individual dendritic branches? This raises the question whether GABAergic inputs are distributed evenly along all the individual branches, or whether there are specific rules for within branch localization? The procedure to test for this is depicted schematically

in figure 6A. In a given dendritic tree each individual dendritic branch is divided into 10 sections of equal length. This is followed by averaging over all dendrites of the tree, whether putative GABAergic inputs are distributed evenly along the individual branches, or whether there are sections of individual branches which receive significantly less or more inputs than others. Even in a situation with GABAercic inputs located predominantly in higher Sholl spheres these might be distributed evenly along the individual branches (Fig 6A, middle panel). By contrast, one could also envision a scenario in which inhibitory inputs might be targeted so that they selectively shunt individual dendritic sub-trees. One possibility would be that higher order dendrites, which are thick and give rise to many lower order dendrites, receive putative GABAergic inputs predominantly at their distal end at the root of the dendritic sub-tree they give rise to, but not at there proximal end which connects these dendrites to other sub-trees (Fig 6A, right panel). By contrast, thin higher order dendrites might receive an even distribution of inhibitory inputs. To test low order thick dendrites and high order thin dendrites separately, all dendrites of any given dendritic tree were divided into two classes, thick dendrites between 0.5 and 1 µm radius and thin dendrites with radii smaller than 0.5 µm. For both classes of dendrites the total surface area and the total surface area contacted by putative GABAergic inputs were determined. The ratio yielded the percentage of dendritic surface contacted by putative GABAergic synapses. This ratio showed little variability for either the thick or the thin dendrites across different animals at a given developmental stage (thick dendrites adult, $4.6 \pm 0.6$ %; thin dendrites adult, $9.3 \pm 0.5$ %; larva thick dendrites $5.4 \pm 0.13$ %; larva thin dendrites $5.7 \pm 0.13$ %; 0.25 %). These values were used to calculate an expected dendritic surface area contacted by putative GABAergic inputs within each of the 10 sections along all individual dendrites of a given class (Fig 6A, left panel). The null hypothesis was that on average, the surface of each of the 10 sections along each of the dendrites was contacted by an equal number of GABAergic inputs, i.e. no preferential targeting of inhibitory synapses was expected along individual branches. Then, the average surface area contacted by GABAergic synapses was determined for each of the 10 sections along the dendrites by analyzing the putative GABAergic input distribution pattern found within the surface reconstruction. Finally, for each section the surface area that was on average contacted by GABAergic terminals was divided by the expected surface area. Consequently, numbers bigger than 1 indicates that within a given section along the dendrites more GABAergic terminals than expected make contact. And vice versa, a
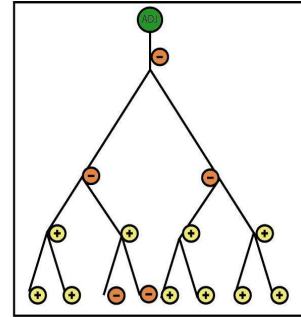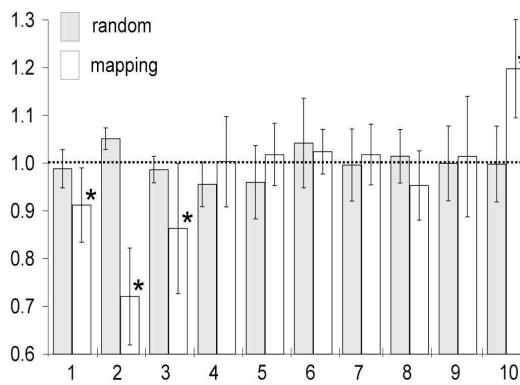
**A1** analysis scheme
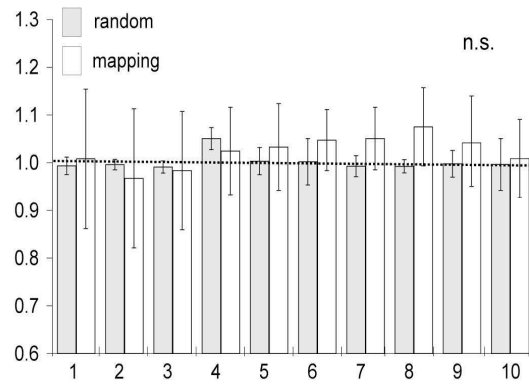
**A2** random within branch distribution

**A3** strategic synapse locations at the roots of low order branches
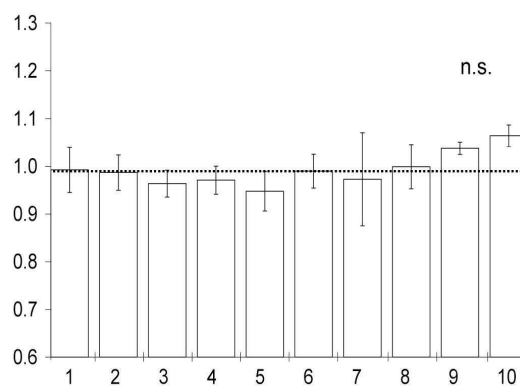
**B** adult MN5 thick dendrites (0.5 - 1.0 µm)

**C** adult MN5 thin dendrites (0.0 - 0.5 µm)

**D** larval MN5 thick dendrites (0.5 - 1.0 µm)

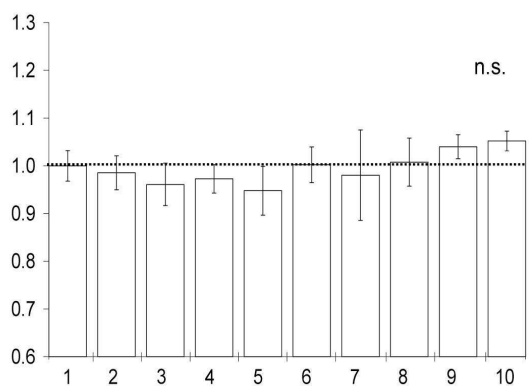**E** larval MN5 thin dendrites (0.0 - 0.5 µm)

**Figure 6.** *Only in the adult MN5 putative GABAergic inputs occur predominantly at the roots of thick low order braches*

(A) describes the logic and the procedure of the analysis shown in B. For analysis each dendrite of a tree is divided into 10 sections of identical length (A1). The hypothesis to test was whether, on average, putative GABAergic inputs are evenly distributed along all 10 sections of the dendrites. Random distribution of excitatory and inhibitory synapses along individual dendrites is schematized in (A2, random within branch distribution). (A3) depicts schematically an example of random distribution in higher order branches, but increased occurrences of GABAergic inputs to the roots of low order branches. To test whether increased input incidences occurred on average in any of the 10 sections (A) along individual branches a four step procedure was conducted. First, all dendrites of a tree were divided into thick low order dendrites (0.5 to 1 µm radius) and thin higher order dendrites (radius < 0.5 µm). Second, for each reconstruction the percentage dendritic surface that was contacted by putative GABAergic inputs was determined separately for thick and for thin dendrites. Third, total dendritic surface was determined for each of the 10 segments along individual dendrites. Fourth, with the null hypothesis of an even distribution the overall percentage GABAergic input and the total surface area in each of the 10 dendritic segments (averaged over all dendrites) were used to calculate the expected surface area contacted by GABAergic terminals within each of the 10 segments, separately for thick and for thin dendrites. Fifth, for each of the 10 segments the measured surface areas contacted by putative GABAergic inputs were determined (averaged over all dendrites, but separately for thick and thin dendrites). And sixth, averaged over all dendrites and four different animals within each of the 10 segments along the dendrites the measured surface area was dived by the expected surface area and plotted for all 10 sections. A y-value larger than one means that within this section averaged over all dendrites more surface than expected is contacted by putative GABAergic inputs. This procedure was conducted separately thick (B, white bars) and thin (C, white bars) dendrites in the adult MN5 and for thick (D, white bars) and thin dendrites in the larva (E, white bars). Error bars represent standard deviation. Asterisks indicate significance (ANOVA, Newman Keuls post hoc test p < 0.01). As additional test a random number generator was used to calculate a random distribution of GABAergic inputs throughout the 10 sections. Inputs were average surface areas contacted by GABAergic terminals, dendritic surfaces, and number of branches as determined experimentally. Randomly generated distributions were plotted for the adult MN5 for thick (B, grey bars) and thin dendrites (C, grey bars) and yielded no significant differences between any of the 10 section along the dendrites.

number smaller than 1 indicates that this specific section along the individual dendrites was contacted by fewer GABAergic terminals than expected. This was done separately for all thick and all thin dendrites within each animal and subsequently averaged over four adult and three larval animals. For thick dendrites in the adult MN5, the number of GABAergic inputs is significantly increased in segment 10 and significantly decreased in segments 1, 2 and 3 (Fig 6B, white bars, ANOVA, Newman Keuls post hoc test p < 0.01). This means that putative inhibitory inputs do not occur randomly along the run of individual thick dendrites (between 0.5 and 1 µm diameter), but by contrast are located with a higher likelihood towards the end of thick dendrites, i.e. at the root of dendritic sub-trees arising from this dendrite but furthest away from other sub-trees. To double test whether such a distribution along individual dendrites could occur randomly we used a random poisson number generator and the same synapse likelihoods and numbers of dendrites as occurring in each of the animals subjected to the analysis. No significant

differences in the occurrence of putative GABAergic inputs were observed along branch sections within thick dendrites in the adult MN5 (Fig 6B, grey bars, ANOVA p = 0.71). For thin dendrites (0 – 0.5 µm diameter) no significant differences were found between any of the 10 sections along each of the dendrites (Fig 6C, white bars, ANOVA p = 0.86), nor did the distribution derived from the confocal data differ from the one derived from random number generation (Fig 6C, grey bars). These data demonstrate that in the adult MN5 only for dendrites with a diameter larger than 0.5 µm specific targeting of putative GABAergic inputs occurs predominantly towards their distal end (Figs 6B, C). By contrast in the larval MN5 no significant targeting to any of the sections within individual dendritic branches was observed (Figs 6D, ANOVA p = 0.14; 6E, ANOVA p = 0.22). Therefore, non-random targeting of putative GABAergic inputs preferentially towards the roots of dendritic sub-trees occurs in the adult flight but not in the larval crawling motoneuron.

In summary, the integration of MN5 into the newly formed flight motor networks during postembryonic development is accompanied by targeting putative GABAergic input synapses to specific sub-dendritic addresses. First, putative inhibitory inputs occur at a higher density at the perimeter of the dendritic field (Fig 4), and second, low order branches are targeted with a higher likelihood at their distal end, which is the root of dendritic sub-trees (Fig. 6). These rules for sub-dendritic distribution of putative GABAergic inputs are not a reflection of varying overall synaptic densities of this transmitter class in the neuropil (Fig 5), but are likely to reflect the targeting of individual presynaptic neurons in a precisely predetermined fashion. This synaptic distribution could be the consequence of molecular targeting mechanisms helping to organize synaptic assembly during metamorphosis. Whether it might also have consequences for the optimization of the neurons' computation efficiency to support the generation of adequate behavior is the question we address with the following computational experiments.

Two concurring ideas exist how GABAergic inputs could be integrated into the sequence of MN5 repetitive firing patterns which ultimately lead to the generation of muscle contraction and therefore behavior. To the one extreme, phasic GABAergic inhibition might prevent the neuron from further spiking and reset the dendrite to a computational ground state to improve precision and repeatability. To the other extreme GABAergic input could be used to modulate the gain of the conversion machinery

which translates a given tonic excitatory synaptic input level into a train of action potentials with controlled frequency. These two examples highlight a fundamental difference on how asynchronous synaptic input might have to be convoluted into a membrane potential transient at the spike generating zone of a neuron. In the first case, the amount of synaptic depression of the neuron should be highly dependent on the degree of temporal input synchronization, and the temporal inaccuracy of synaptic drive (which is inherent to naturally occurring synaptic input) should be reproducibly filtered to produce the peak deflection of membrane potential at a defined delay with respect to the center of the distribution of synaptic activation. The sequence of synaptic firing on the level of individual synapses should have a minor impact. We hypothesize that this should be the role for GABAergic input to the adult MN5. Highly synchronized cycle by cycle inhibition should ensure the occurrence of tightly timed single spikes once per wing beat, and it should reset the dendritic tree to a computational ground state after every wing beat. By contrast, for the latter case of a larval slow motorneuron, synaptic firing should translate into a broad shoulder of membrane deflection, which is rather invariant to the degree of input synchronicity. Precise timing of the peak amplitude in membrane potential change would therefore be irrelevant. We hypothesize that this should be the case for GABAergic inputs to the larval MN5, because it innervates a slowly contracting muscle, and during crawling behavior it fires tonic bursts of action potentials, with no demand on spike time precision within each burst.

To which extent these properties are due to active membrane conductances or whether a neuron might as well employ its passive integration properties of its dendritic geometry in parallel with specific distribution rules for synaptic loci, is an unresolved question. We therefore examined how the dendritic geometry and synaptic distribution characteristics as determined above influence the characteristics of a synaptically driven transient membrane depolarization in a passive dendritic tree.

As the first computational experiment we distributed 50, 100, and 200 synapses onto a passive multi-compartment model of the dendritic tree of a larval respectively adult MN5 in accordance to the determined GABAergic synapse distribution pattern as described above (see methods). Each synapse was set to fire once during a simulation iteration. The time point of firing onset was randomized for each individual synapse, so that the temporal distribution of the synaptic activation sequence followed a Gaussian distribution with a given width (sigma, see methods). Simulations were run with 8 different sigmas (0.1, 0.2, 0.4, 0.8, 1.6, 3.2, 4.8, 6.4ms) to compare different degrees of

input synapse firing synchronization, with the distributions' center at 10ms after simulation onset. To account for both, different synapse firing sequences as occurring at any sigma larger than 0, and also for different sites of activated synapses within the dendritic tree, each simulation was run for 10 independently drawn synapse loci and 20 different temporal sequences of activation, resulting in 200 simulations per synapse number and sigma. In figure 7, the different degrees of input synapse firing synchronization are depicted in different colors. For the larval dendritic tree (Fig 7A1) and 50 GABAergic synapses (Fig 7A1, left panel), different degrees of input synchronization (sigma) do not result in different maximum depolarization amplitudes at the root of the dendritic tree. In contrary, the peak amplitudes of synaptically evoked depolarizations are mostly intermingled with regard to amplitude size (y-axis) and time of peak depolarization (x-axis). By contrast, for the adult dendritic tree and 50 synapses (Fig 7B1, left panel) the resulting depolarization amplitudes segregate for different degrees of input synchronization. This indicates that the adult MN5 evaluates the degree of input synapse firing synchronization to affect membrane depolarization more than the activation sequence of the individual synapses or different loci within the GABAergic synapse pool. Figures 7A2 and B2 show the respective boxplots for the distributions depicted in 7. Increasing the number of active synapses to 100 and 200 lead to a more pronounced segregation of maximum depolarization amplitude in the adult dendritic tree (Figs 7B1 and B2, middle and right panel). By stark constrast, increasing the number of activated GABAergic synapses on the larval dendritic tree to 100 and 200 increases the overlap of depolarization amplitudes of different synaptic synchronization (Figs 7A1and 2, middle and right panel).

Therefore, maximum depolarization amplitude is clearly more strongly affected by input firing synchronization in passive models of the adult as compared to the larval dendritic tree. The spread of maximum depolarization amplitudes over all synapse localizations, activation sequences and sigmas however are similar for the larval and the adult dendritic tree for any given number of synapses (Figs 7A1, A2, B1, B2). To test whether the higher sensitivity to input synchronization of the adult MN5 is simply caused by a different ratio of synapse number and total tree length, all simulations were repeated with a scaled larval dendritic geometry to match the adults dendritic length (see methods; Figs 7C1 & 2). Also in a scaled larval MN5, for 50 synapses different sigmas do not yield a segregation of the maximum depolarizations (Fig 7C1 & 2), but rather emphasizes the dependency on synaptic firing sequence and specific synapse loci.
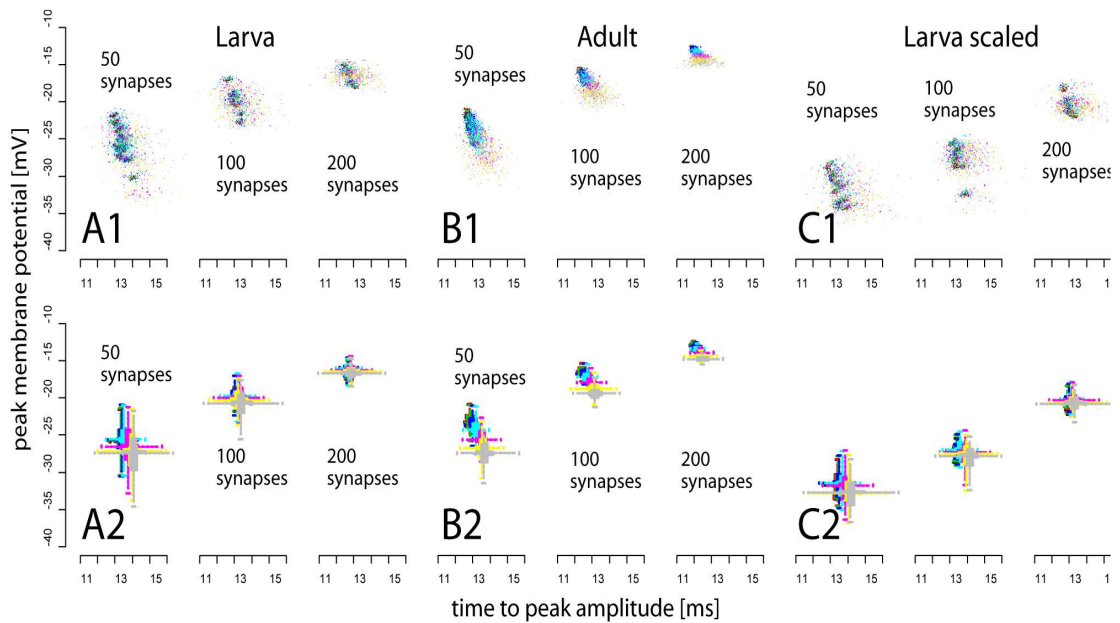
**Figure 7.** *Asynchronous synaptic inputs at putative GABAergic sites onto the larval and adult dendritic tree are summated by purely passive integration properties to support a behavioraly adequate response.*

Plotted are the results of computational modeling, showing the peak depolarization response over time to peak at the axo-dendritic junction as the result of asynchronous synaptic input at putative GABAergic sites onto the larval (A) and adult (B) MN5. (C) shows the response of a larval tree which is scaled to the same length as the adult tree. 50, 100, and 200 synapses where distributed according to the earlier described synaptic patterns (figure 4D, E; 10 iterations) and their temporally asynchronous activation (20 iterations) was drawn from a Gaussian distribution with different widths (sigma equals 0.1 (black), 0.2 (red), 0.4 (green), 0.8 (dark blue), 1.6 (light blue), 3.2 (pink), 4.8 (yellow) and 6.4 (grey) milliseconds). A1, B1 and C1 show the single data points and A2, B2 and C2 are the corresponding box plots showing the distribution characteristic, whereas the dotted lines represent the total spread of the distribution, the solid bars represent the space between lower and upper quantile and the intersection of the dotted lines demark the median value. In the larval tree (A), the peak response is mostly independent of the degree of synchronicity of synaptic activation, as the distribution of peak responses evoked by different synaptic synchronicities interleave to a high degree. In the adult tree (B) however, a synchronicity dependent segregation of peak membrane depolarization can be clearly observed. This answer characteristic is not just due to the longer adult dendritic tree, as the scaled larval tree convolutes synaptic input in a qualitatively identical fashion as the unscaled larval tree, only the absolute depolarization value is lower.

This set of modelling results strongly suggests that the combination of dendritic geometry and specific synapse distribution on the larval dendritic tree evaluates the activation sequences to affect maximum depolarization rather than different firing synchronizations. In addition, in a scaled larval tree the spread of maximum depolarization amplitudes over all synapse localizations, activation sequences and sigmas is almost twice as large as compared for the adult dendritic tree for any given

40

number of synapses (compare Figs 7B1, C1; B2, C2). Therefore we conclude that dendritic geometry is indeed supporting the above hypothesized behavioral request on the computational properties of the larval versus the adult dendritic tree in passive models.

To tease apart the specific contribution of the topology of the dendritic tree rather than the combined effect of branch pattern and synapse distribution, we randomized the positioning of synapses in regard to the midline length of the dendritic tree (Fig. 8). In the case of the larval tree, we now changed the larval response to a synchronization dependent segregation of the maximum amplitude of the membrane depolarization for 50 synapses (Fig 8A1, A2), and this is augmented with increased synapse numbers (100 synapses: B1, B2; 200 synapses: C1, C2) Randomizing synapse distribution in the adult tree however does qualitatively not affect the response to synaptic input in comparison to the GABAergic synapse distribution (Fig.8 A3/4 - C3/4). Interestingly, comparing the response distributions between larval and adult randomized synapse localization reveals that the degree of synchronization dependent discrimination of synaptic activation is less in the larval tree.

These findings strongly suggest that in the case of GABAergic activation in the larval dendritic tree, both specific synapse distribution and tree topology filter the synaptic activation in co-orperation. Purely passive mechanisms enable the tree to evaluate the absolute number and identity of active synapses in synaptic volleys within a period between 0.1 and 6.4 milliseconds. The adult tree however mainly filters synaptic input to strongly reflect the degree of synchronicity in a graded response profile to a increased timely input coherence.

Synapse localization probabilities as determined experimentally were transformed into a discrete map of synaptic localizations (see methods). As demonstrated above (Figs 7A1, A2) different degrees of input synapse firing synchronization does not segregate into different amplitudes of maximum depolarization at the larval dendritic tree of MN5. However, with random synapse distributions some separation of the maximum depolarization amplitudes is observed when the number of activated synapses is increased from 50 to 100 or even to 200 (Fig 8A1-C2). Repeating the same simulation experiments with synapse distributions as determined experimentally for GABAergic inputs for the larval MN5 yields no differences in the maximum depolarization amplitudes, no matter whether 50, 100 or 200 (Fig 8A1-C2) synapses are
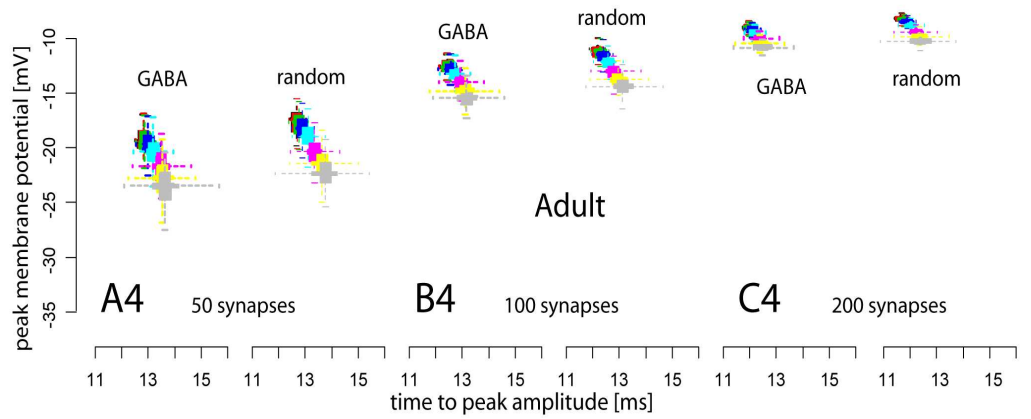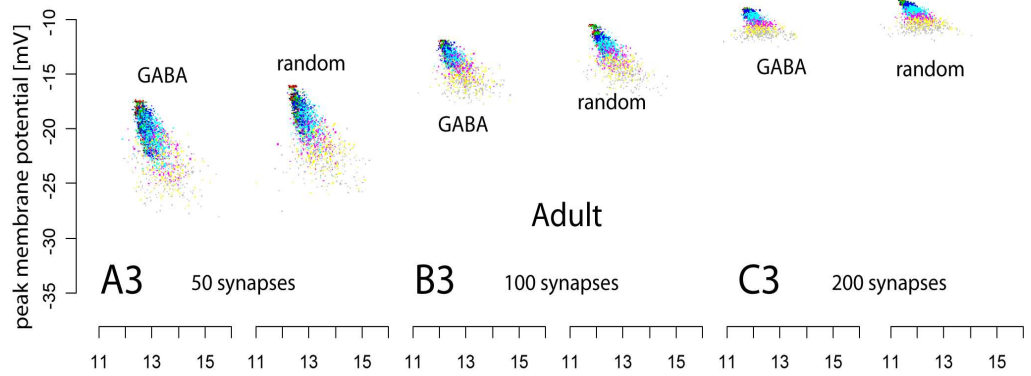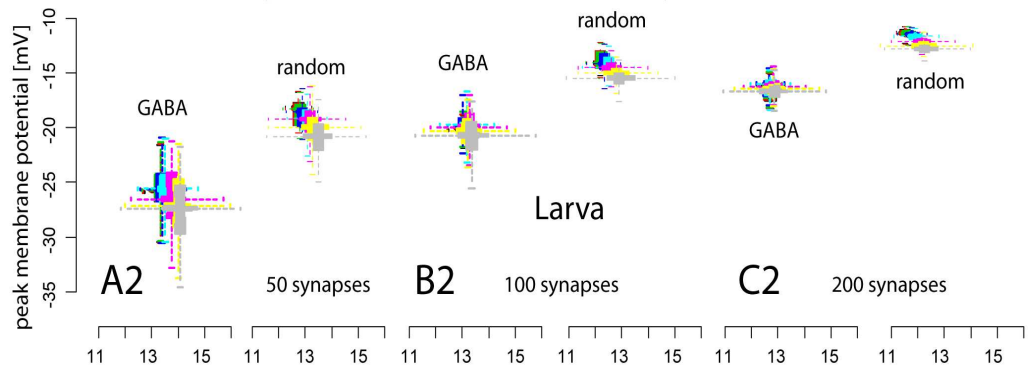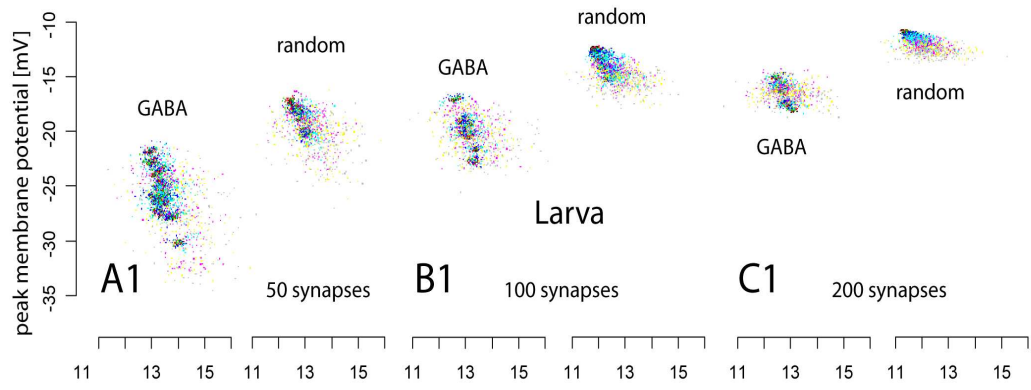
**Figure 8.** *Comparison of the effect of GABAergic versus randomized synaptic distribution patterns on the passive integration of synaptic activation.*
Peak membrane depolarizations at the axo-dendritic junction were determined with computational experiments modeling passive dendritic integration and are depicted as described in figure 7. In case of the larval tree, random and GABAergic synapse distributions lead to distinct answer profiles for 50 (A), 100 (B) and 200 (C) synapses. GABAergic synapse loci do not allow distinguishing between different degrees of synchronicity of synaptic activation, as the corresponding distributions of resulting peak amplitudes overlap extensively (A1, B1, C1, left panel; corresponding box plots are shown in (A2, B2, C2, left panel)). In contrast, for a randomized synaptic localization with regard to the midline length of the dendritic tree, the peak depolarization responses segregate into less overlapping domains in response to synaptic activation with different degrees of synchronization (A1, B1, C1, right panel; corresponding box plots are shown in (A2, B2, C2, right panel)). In the adult tree, GABAergic and randomized synaptic loci lead to indistinguishable patterns of peak responses in terms of the segregation into depolarization domains as result to different activation synchronicities (A3, B3, C3, left panel; corresponding box plots are shown in (A4, B4, C4, left panel)). The random distribution of synapses however seems to lead to a slightly higher depolarization answer (A3, B3, C3, right panel; corresponding box plots are shown in (A4, B4, C4, right panel)). Temporal synaptic firing synchronicities follow a Gaussian distribution with different widths are depicted color coded (sigma equals 0.1 (black), 0.2 (red), 0.4 (green), 0.8 (dark blue), 1.6 (light blue), 3.2 (pink), 4.8 (yellow) and 6.4 (grey) milliseconds).

activated. This demonstrates that not only dendritic geometry but also the synapse distribution patterns for GABAergic inputs are designed to not evaluate different degrees of synaptic input synchronization. In addition, experimentally derived synapse localization patterns yield less overall depolarization amplitudes as compared to randomly distributed synapses in the larval MN5 (Fig 8). And finally, maximum depolarization at the root of the larval dendritic tree varies approximately twice as much depending on the sequence of activation in simulations with experimentally derived synapse localization as compared to random synapse distributions (Fig 8).

For the adult MN5, no experimentally derived distributions for GABAergic synapses and random synapse distributions do not yield any differences with respect to the effectiveness of different input synapse synchronizations, in both cases different sigmas cause different amplitudes of maximum depolarizations (as shown for randomly distributed synapses in figure 8A3-C4). However, distributing GABAergic synapses according to the rules shown in figure 4 yields a slightly higher independence from the sequence of synapse activation (data not shown). Therefore, pushing synapses towards the perimeter of complex dendritic trees decreases the need for controlling which presynaptic neuron fires first, but does not decrease the need for all presynaptic neurons firing within a certain narrow time window.

## 2.5 Discussion

The results demonstrate that postembryonic changes in the function of the identified motoneuron MN5 are accompanied by functional dendritic architecture remodeling and by changes in the sub-dendritic distribution patterns of putative GABAergic input synapses. Multi-compartment simulations in solely passive models suggest that dendritic architecture of the adult flight motoneuron is tuned towards differentiation between different levels of temporal synchronicity of synaptic input, whereas dendritic architecture in the larval MN5 disregards different levels of input synchronicity but evaluates total number of activated synapses and their specific identity. The larval MN5 receives an even distribution of GABAergic inputs through all Sholl spheres and also along individual dendritic branches. By contrast, after MN5 has developed into an adult flight motoneuron, it receives a higher overall density of putative GABAergic inputs and more putative GABAergic inputs in higher Scholl spheres at the perimeter of the dendritic field. In addition, putative GABAergic inputs close to the spike generating zone at the axon are preferentially targeted to the roots of dendritic sub-trees. By measuring synapse densities in several areas in the larval and adult neuropile, we could exclude that the synapse distribution pattern we find is a simple reflection of neuropil structure. Therefore we conclude that there is sub-dendritic targeting of inputs onto the adult motoneuron. The computational function of this sub-dendritic synapse targeting in the adult MN5 however remains unclear.

### 2.5.1 Sub-dendritic synapse targeting

The overall densities of GABAergic terminals are not statistically different between the larval and the adult motor neuropil or between different parts of the adult neuropil. Three classes of GABAergic interneurons are known to make connections with motoneurons in the insect thoracic ventral nerve cord, local spiking interneurons (Watson and Burrows, 1998), intersegmental spiking interneurons (Watson and Laurent, 1990), and non-spiking intersegmental interneurons (Wildmann et al., 2002). In accordance to our findings which demonstrate a homogenous distribution of GABAergic terminals, the projections of these classes of neurons are not restricted to specific parts of the motor neuropil. Therefore, specific recognition mechanisms must exist for GABAergic interneurons to specifically distinguish between the larval and the adult dendrites of MN5 and between different sub-domains of the adult dendritic tree.

In principle, two categories of mechanisms could account for sub-dendritic synapse targeting. First, 'activity dependent site-specific pruning' of dendrites, i.e. initial synaptic inputs form non-selectively through the dendritic field and sub-dendritic specificity is established by experience induced elimination of inappropriate inputs, or by activity dependent site specific synapse maintenance. Alternatively, sub-dendritic targeting might be accomplished in an experience independent manner by the presence of molecular signals on the appropriate dendritic compartments. Experience guided sub-cellular synapse elimination has been reported to confine inhibitory glycinergic inputs to the somata of auditory interneurons in rodents (Kapfer et al. 2002). By contrast, specific sub-cellular targeting of two different types of major GABAergic synapses along the perisomatic and the dendritic domains of pyramidal neurons in visual cortex (Freund and Buzsaki, 1996) does not rely on experience dependent thalamic input (DiCristo et al., 2004). Sub-dendritic targeting of inhibitory inputs through different dendritic domains of MN5 is most likely also established in an experience independent manner, because adult synapse distribution patterns are already established at the day of adult emergence, and the pupae can not fly. However, at current we can not exclude the possibility that flight motor network activity in the pupal nervous system might occur at amplitudes sub-threshold to cause muscle contractions, but still instructive for restricting synapse locations to specific parts of the dendritic field. The central motor network for flight is established at least two days before adult emergence as demonstrated by pharmacological induction of flight-like motor pattern (Kinnamon et al., 1984; Vierk, unpublished results). However, adequately patterned sensory feedback can not occur within the pupal cuticle and no flight muscle twitches were observed during normal development, leaving molecular cues which denote sub-dendritic domains the more parsimonious explanation.

It is well established that the cellular polarization into axon and dendrites is manifested early during development by the presence of different sets of cell surface molecules (Craig and Baker, 1994). However, dendrites themselves can be further polarized in apical or basolateral domains for instance, and it has been suggested that individual dendritic segments may have distinct molecular identities (Horton and Ehlers, 2003). Furthermore, in cultured hippocampal neurons somatodendritic targeting of Kv 2.1 potassium channels has been demonstrated (Lim et al., 2000), whereas other experiments show that the AMPA receptor density is progressively increased towards the distal end of hipoocampal CA1 pyramidal neurons (Magee and Cook, 2000;

Andrasfalvy and Magee, 2001), suggesting sub-dendritic specialization in the proximal to distal dimension. Our findings demonstrate a proximal to distal dendritic polarity as an evolutionary conserved principle, found in neurons as different as insect motoneurons and mammalian pyramidal neurons. At present it remains unclear which extrinsic or intrinsic signals, such as neurotrophins (Huang and Reichard, 2003) and cytoskeletal regulatory proteins may establish and maintain proximal to distal dendritic polarity.

## 2.5.2 Function of dendritic architecture remodeling

Many insect muscles with well characterized functions are innervated by few individually identified motoneurons, allowing to relate dendritic architecture and input synapse distributions directly to behavioral function. The larval crawling motoneuron innervates a slowly contracting body wall muscle (Duch et al., 2000). In invertebrates the contraction slopes of such muscles are mostly independent of brief changes in motoneuron spiking frequency and motoneuron spike timing (Morris and Hooper, 1998; Hooper et al., 2007). By contrast, the adult flight MN5 innervates a fast contracting flight muscle, which twitches once per MN5 spike, contracts 25 times per second during flight, and flight behavior relies on sub-millisecond single contraction precision (Tu and Daniel, 2004). Therefore, the computational demands for precise coding of synaptic input synchronicity are much higher in the adult as compared to the larval dendritic tree of MN5. Correspondingly, our multi-compartment simulations demonstrate that depolarization timing and amplitude close to the spike initiating zone of the adult MN5 passive dendritic tree vary strongly with input synchronicity. By contrast, input synchronicity is not coded in depolarization amplitude or timing close to spike initiation of the larval MN5 passive dendritic tree. This suggests that dendritic architecture changes as occurring during metamorphosis are well suited to sub-serve the changing behavioral function of MN5. Functional roles of dendritic shape for behaviorally relevant computations have previously been demonstrated in few systems only (London and Haeusser, 2005), for instance in directional sensitive information processing in fly visual interneurons (Single and Borst, 1998). To the best of our knowledge this study provides the first evidence for postembryonic dendritic shape changes that underlie behaviorally relevant dendritic computations. However, passive multi-compartment models are certainly a simplification. MN5 contains dendritic calcium conductances (Duch and Levine, 2002), and active membrane properties may change the

computational properties of dendrites significantly (London and Hausser, 2005). Furthermore, our simulations operate with the same conductance for all synapses, but in real life a variety of pre- and postsynaptic mechanisms can alter synaptic strength. Nevertheless, this reductionist approach carves out dendritic architecture as a potentially important variable for motor behavior specific computations of synaptic input timing.

In MN5 increasing demands on input synapse integration, as occurring during the development from a slow crawling into a fast flight motoneuron, are accompanied by the establishment distinct of sub-dendritic input synapse distributions. Functional significance for segregation of different types of synaptic input to different sub-dendritic domains has been suggested for GABAergic innervation of pyramidal cells (Pouille and Scanziani, 2001), and some evidence for behavioral significance has been found in an identified locust visual interneuron involved in collision avoidance during flight (Gabbiani et al., 2002). We find even more intricate rules for sub-dendritic input distributions in the adult flight MN5, but the behavioral consequences remain unclear. Multi-compartment models with random versus real distributions of putative GABAergic input synapses do not reveal different input output computations, but only slight differences in depolarization amplitude and in the sensitivity to the sequence of presynaptic synapse firing. Both can easily be explained by attenuation of depolarization amplitude along the path of the dendrites, which must be larger with real inputs because these occur predominantly at the perimeter of the dendritic tree. However, this does not exclude the possibility that distinct computational properties of synapse distribution patterns as observed in the adult flight MN5 might be revealed as soon as active membrane conductances or synapses with different transmitter classes are added to the models. By contrast, in the larval MN5 input synapse distributions as observed in this study change the computational properties of the passive tree as compared to random synapse distributions. Using experimentally derived distributions of GABAergic synapses caused the passive dendritic tree to sum synaptic inputs at the root of the dendritic tree almost completely invariantly from temporal input synchronizations between sigma 0 and sigma 6400 (sigma in µs describing the mean of a Gaussian distribution). Such invariance is well suited for the behavioral function of the larval MN5 which is to produce periodically occurring bursts with little spike time precision to induce slow contractions of body wall muscles during slow crawling movements of the larva (Duch and Levine, 2000).

During recent years, with increasing knowledge on dendritic properties, the role of individual neurons has evolved conceptually form that of a simple integrator of synaptic input to a much more sophisticated processor converting binary synaptic input into analogue variables, like postsynaptic membrane potential or intracellular calcium levels, which in turn, can be subject to computations like filtering, gain control, normalization, amplification, multiplication and thresholding (Sheperd, 1992; Koch, 1999). The fact that rules seem to exist for the spatial distribution of inputs on dendritic fields, and that such distributions are manifested in a stage-specific manner during postembryonic life adds an additional level of complexity to our understanding of brain function. Computations in neural circuitry might not only depend on which neuron is connected to which other neurons, but also on intricate rules for sub-dendritic spatial distributions of these connections, and errors in the development and maintenance of such rules might contribute to neurological disease. Evidence for linking synaptic input on distal dendrites with behaviorally relevant computations comes from transgenic mice with a forebrain restricted HCN1 (H-current) deletion. In CA1 pyramidal cells H-current is restricted mainly to distal dendrites (Magee, 1998). In knock-outs, on the cellular level, distal synaptic inputs into pyramidal cells and LTP of these synapses is enhanced, and on the behavioral level these mice exhibited increased performance in hippocampus dependent memory tasks (Nolan et al., 2004). This indicates functional relevance of independent regulation of synaptic input to different dendritic sub-domains. Unraveling the mechanisms for sub-dendritic synapse localization in identified insect motoneurons might allow testing the behavioral function of intricate synapse localization rules by manipulations on the single neuron level.

## 2.6 References

Andrasfalvy BK, Magee JC (2001) Distance-dependent increase in AMPA receptor number in the dendrites of adult hippocampal CA1 pyramidal neurons. J Neurosci 21:9151-9159.

Bell RA, Joachim FA (1976) Techniques for rearing laboratory colonies of tobacco hornworms and pink bollworms. Ann Entomol Soc Am 69:365– 373.

Burrows M (1996) The Neurobiology of an Insect Brain. Oxford University Press, Oxford UK.

Chen BL, Hall DH, Chklovskii DB (2006) Wiring optimization can relate neuronal structure and function. PNAS 103:4723-4728.

Chklovskii DB, Schikorski T, Stevens CF (2000) Wiring optimization in cortical circuits. Neuron 34:341-347.

Consoulas C, Duch C, Bayline RJ, Levine RB (2000). Behavioral transformations during metamorphosis: remodeling of neural and motor systems. Brain Res Bull 15: 571-583.

Craig AM, Banker (1994) Neuronal polarity. Annu Rev Neurosci 17:267310.

Di Christo G, Wu C, Chattopadhyaya B, Ango F, Knott G, Welker E, Svoboda K, Huang ZJ (2004) Subcellular domain-restricted GABAergic innervation in primary visual cortex in the absence of thalamic inputs. Nat Neuroscience 7:1184-1186.

Duch C, Levine RB (2000) Remodeling of membrane properties and dendritic architecture accompany the postembryonic conversion of a 'slow' into a 'fast' motoneuron. J Neurosci 20:6950-6961.

Duch C, Levine RB (2002). Changes in calcium signaling during postembryonic dendritic growth in Manduca sexta. J Neurophysiol 87(3):1415-25.

Duch C, Mentel T (2004). Stage-specific activity patterns affect motoneuron axonal retraction and outgrowth during the metamorphosis of Manduca sexta. Eur J Neurosci 7(5):945-62.

Evers JF, Schmitt S, Scholz M, Duch C (2005) New frontiers in functional neuroanatomy: precise automatic reconstruction from confocal image stacks. J Neurophysiol 93:2331-2342.

Evers JF, Muench D, Duch C (2006) Developmental relocation of presynaptic terminals along distinct types of dendritic filopodia. Dev Biol 297:214-27.

Gabbiani F, Krapp HG, Koch C, Laurent G (2002) Multiplicative computation in a visual neuron sensitive to looming. Nature 420(6913):320-4.

Hohensee S, Bleiss W, Duch C (2007) Correlative electron and confocal microscopy assessment of synapse localization in the central nervous system of an insect. J Neurosci Methods in press.

Hooper SC, Guschlbauer C, von Uckerman G, Bueschges A (2007) Different motor neuron spike patterns produce contractions with very similar rises in graded slow muscles. J Neurophys 97:1428-1444.

Horton AC, Ehlers MD (2003) Neuronal polarity and trafficking. Neuron 40:277-95.

Huang EJ, Reichardt LF (2003) TRK receptors: Roles in neuronal signal transduction. Annu Rev Biochem 72:609-642.

Kapfer C, Seidle AH, Schweizer H, Grothe B (2002) Experience-dependent refinement of inhibitory inputs to auditory coincidence-detector neurons. Nat Neurosci 5:247-253

Kinnamon SC, Klaassen LW, Kammer AE, Claassen D (1984) Octopamine and chlordimeform enhance sensory responsiveness and production of the flight motor pattern in developing and adult moths. J Neurobiol 15:283-293.

Koch C, Segev I (2000) The role of single neurons in information processing. *Nat Neurosci* 3 Suppl:1171-1177.

Lim ST, Antonucci DE, Scannevin RH, Trimmer JS (2000) A novel targeting signal for proximal clustering of the Kv2.1 K+ channel in hippocampal neurons. Neuron 25:385-397.

Libersat F, Duch C (2002) Morphometric analysis of dendritic remodeling in an identified motoneuron during postembryonic development. J Comp Neurol 450(2):153-166.

Libersat F, Duch C (2004) Mechanisms of dendritic maturation. Mol Neurobiol 29(3):303-320.

London M, Haeusser M (2005) Dendritic computation. Annu Rev Neurosci 28:503-532.

Magee JC. (1998) Dendritic hyperpolarization-activated currents modify the integrative properties of hippocampal CA1 pyramidal neurons. J Neurosci 18(19):7613-7624.

Magee JC, Cook EP (2000) Somatic EPSP amplitude is independent of synapse location in hippocampal neurons. Nat Neurosci 3:895-903

Morris LG, Hooper SL (1998) Muscle response to changing neuronal input in the lobster (*Panulirus interruptus*) stomatogastric system: slow muscle properties can transform rhythmic input into tonic output. J Neurosci 18: 3433–3442.

Nolan MF, Malleret G, Dudman JT, Buhl DL, Santoro B, Gibbs E, Vronskaya S, Buzsáki G, Siegelbaum SA, Kandel ER, Morozov A (2004) A behavioral role for dendritic integration: HCN1 channels constrain spatial memory and plasticity at inputs to distal dendrites of CA1 pyramidal neurons. Cell 119(5):719-732.

Pouille F, Scanziani M (2001) Enforcement of temporal fidelity in pyramidal cells by somatic feed-forward inhibition. Science 293:1159-1163.

Rabinowitch I, Segev I (2006) The interplay between homeostatic synaptic plasticity and functional dendritic compartments. J Neurophysiol 96: 276-283.

Reinecke JP, Buckner JS, Grugel SR (1980) Life-cycle of laboratory-reared tobacco hornworms, *Manduca sexta*—study of development and behavior, using time-lapse cinematography. Biol Bull 158:129–140.

Schmitt S, Evers JF, Scholz M, Duch C, Obermayer K (2004) New methods for the computer assisted 3D reconstruction of neurons from confocal image stacks. Neuroimage 23:1283-1298.

Sholl DA (1953) Dendritic organization in the neurons of the visual cortex and motor cortices of the cat. J Anat (Lond) 87:387–406.

Single S, Borst A (1998) Dendritic integration and its role in computing image velocity. Science 281:1848-1850.

Somogyi P, Tamas G, Lujan R, Buhl EH (1998) Salient features of synaptic organisation in the cerebral cortex. Brain Res Brain Res Rev 26:1113-135.

Stepanyants A, Hof PR, Chklovskii DB (2002) Geometry and structural plasticity of synaptic connectivity. Neuron 34:275-288.

Stepanyants A, Chklovskii DB (2005) Neurogeometry and potential synaptic connectivity. Trends Neurosci 28:387-394.

Stricker C, Field AC, Redman SJ (1996) Changes in quantal parameters of EPSCs in rat CA1 neurones in vitro after the induction of long-term potentiation. J Physiol 490 ( Pt 2):443-454

Stricker C, Field AC, Redman SJ. (1996) Statistical analysis of amplitude fluctuations in EPSCs evoked in rat CA1 pyramidal neurones in vitro. J Physiol 490 ( Pt 2):419-441.

Tissot M, Stocker RF (2000) Metamorphosis in Drosophila and other insects: the fate of neurons throughout the stages. Prog Neurobiol 62: 89-111.

Tolbert LP, Matsumoto SG, Hildebrandt JG (1983) Development of synapses in the antennal lobes of the moth *Manduca sexta* during metamorphosis. J Neurosci 3(6):1158-1175

Tu MS, Daniel TE (2004) Submaximal power output from the dorsolongitudinal flight muscles of the hawkmoth *Manduca sexta*. J Exp Biol 207:4651-4662.

Watson AHD, Burrows M (1987) Immunocytochemical and pharmacological evidence for GABAergic spiking local interneurons in the locust. J Neurosci 7:1741-1751.

Watson AHD, Laurent G (1990) GABA-like immunoreactivity in a population of locust intersegmental interneurones and their inputs. J Comp Neurol 302:761-767.

Wildman M, Ott SR, Burrows M (2002) GABA-like immunoreactivity in nonspiking interneurons of the locust metathoracic ganglion. J Exp Biol 205:3651-3659.